

**LOCALIZED CORROSION BEHAVIOUR OF Cu-LEAN AA 7003
EXTRUSIONS**

**LOCALIZED CORROSION BEHAVIOUR OF Cu-LEAN AA 7003
EXTRUSIONS**

By

CHARANYA KRISHNAN

A Thesis

Submitted to the School of Graduate Studies

In Partial Fulfillment of the Requirements

For the Degree of

Master of Applied Science

McMaster University

© Copyright by Charanya Krishnan, June 2011

MASTER OF APPLIED SCIENCE (2011)
(Materials Science and Engineering)

McMaster University
Hamilton, Ontario

TITLE: Localized Corrosion Behavior of Cu-lean AA 7003 Extrusions

AUTHOR: Charanya Krishnan, B.E (Anna University)

SUPERVISOR: Dr. Joseph Kish

NUMBER OF PAGES: iii, 82

ABSTRACT

A study was undertaken to achieve a better understanding of the key microstructure-performance relationships involved with the intergranular corrosion and exfoliation corrosion of Cu-lean AA7003 alloy extrusions, as a function of the heat-treated condition. The heat treatments of interest in this study include the naturally-aged T4 condition, representing the as-extruded condition, an artificially-aged T6 condition, representing a post-weld stress-relief condition, and an artificially-aged automotive paint-bake cycle condition. The influence of heat treatment on the resultant microstructure is characterized using light optical microscopy, coupled with image analysis, and electron (scanning & transmission) microscopy, coupled with energy dispersive spectroscopy. The influence of heat treatment on the corrosion behaviour is characterized using anodic polarization measurements and ASTM standardized testing to evaluate the susceptibility resistance to intergranular corrosion (ASTM G110) and exfoliation corrosion (ASTM G34).

The cross-sectional (LT-ST & L-ST) microstructures of all three heat treatments consist of a fibrous, non-recrystallized grain structure in the interior, and a coarse recrystallized grain structure at the exterior surface. Both grain structures are slightly elongated along L-direction. The grain size distribution and grain aspect ratio distribution is weakly dependant on the heat treatment applied, and on the orientation plane. Among the two artificial aging, the T6 (post-weld stress-relief) condition has the higher micro-hardness (yield strength), as it has higher density (volume fraction) of the strengthening MgZn₂-type precipitates (η , η' and their GP zones) within the Al matrix grains.

Anodic polarization measurements show a more negative corrosion potential (E_{corr}) for the two artificially aging heat-treated conditions. The shift is believed to be due to the micro-galvanic cell activity established between the more noble Al matrix grains and the more active strengthening MgZn₂-type precipitates within the Al matrix grains, which have a significantly increased surface area (volume fraction) in the artificially-aged condition. A similar, single breakdown potential (E_b) corresponding to a pitting potential (E_{pit}) is observed, regardless of the heat-treated condition. The similar potential is believed to be due to localized breakdown of the passive film at the periphery of coarse second phase intermetallic particles (Al₃Fe), which remain unaffected by artificial aging.

Of the three heat-treated conditions studied, the T6 condition exhibits the lowest susceptibility to both intergranular corrosion and exfoliation corrosion. The lower susceptibility is believed to be due to the lack of any Cu enrichment in across the grain boundary region (either in the solute depleted zone or in the generic Mg(Zn,CuAl)₂ grain boundary precipitates). This lack of enrichment is believed to produce a smaller micro-galvanic cell activity across the grain boundary region, as compared to that produced when Cu is enriched across the grain boundary region, particularly in the Solute depleted zone (SDZ).

ACKNOWLEDGEMENTS

I would first like to thank my supervisor, Dr. Joey Kish for his continuous encouragement, suggestions and feedback, which helped kept me motivated for the past two years. I thank him for providing me a great opportunity to work with him and learn from this field of corrosion science. It would have been impossible to me to finish this thesis without his support and patience.

Next, I would like to thank the technical staff, including Connie Barry, Doug Culley, Ed McCaffery, John Rodda, and administrative staff within the Department of Materials Science Engineering (MSE). Moreover, I would like to thank the technical staff, including Chris Butcher, Fred Pearson, Glynis deSilveira, and Steve Koprlich from Brockhouse Institute of Material Research (BIMR) for their assistance and valuable suggestions.

The financial support provided by the Initiative for Automotive Manufacturing Innovation (iAMI) and General Motors of Canada Limited is greatly appreciated. I would like to thank also Alex Graf and Kevin Gong of Alcan Products Corporation for providing me with the AA7003 extruded bumper beam for corrosion testing.

A special note of thanks is extended to all my friends, especially Mehdi Taheri and Stephen Jones, for being my mentors and helping me through difficult times. Finally, I would like to thank my parents for their unconditional love and support throughout my life.

TABLE OF CONTENTS

TABLE OF FIGURES	viii
1.0 INTRODUCTION	1
2.0 LITERATURE REVIEW.....	3
2.1 ALLOY MICROSTRUCTURE	3
2.1.1 INTERMETALLICS.....	3
2.1.2 DISPERSOIDS	5
2.1.3 STRENGTHENING PARTICLES	7
2.2 SECOND PHASE ELECTROCHEMICAL REACTIVITY	11
2.3 CORROSION PROPERTIES OF AA7XXX ALLOYS.....	13
2.3.1 PITTING CORROSION	13
2.3.2 INTERGRANULAR CORROSION.....	15
2.4 SUMMARY	22
3.0 RESEARCH OBJECTIVES	23
4.0 EXPERIMENTAL DETAILS.....	25
4.1 AA7003 EXTRUDED BUMPER BEAM.....	25
4.2 HEAT TREATMENTS.....	27
4.3 MICROSTRUCTURE EXAMINATION	28
4.4 ANODIC POLARIZATION MEASUREMENTS.....	30
4.5 INTERGRANULAR CORROSION TESTING	31
4.6 EXFOLIATION CORROSION TESTING.....	33
5.0 RESULTS	35
5.1 METALLOGRAPHIC EXAMINATION	35
5.2 SEM/EDS EXAMINATION OF SECOND PHASE PARTICLES	38
5.3 STEM/EDS EXAMINATION OF GRAIN BOUNDARIES.....	41
5.4 MICROHARDNESS MEASUREMENTS	42
5.5 ANODIC POLARIZATION MEASUREMENTS	44
5.6 ASTM G110 – INTERGRANULAR COROSION TEST.....	47
5.7 ASTM G34 – EXFOLIATION COROSION TEST	50

6.0	DISCUSSION.....	54
6.1	EFFECT OF HEAT TREATMENT ON MICROSTRUCTURE.....	54
6.2	EFFECT OF HEAT TREATMENT ON CORROSION BEHAVIOUR.....	59
7.0	CONCLUSIONS	65
8.0	REFERENCES	70
	APPENDIX 1.....	77
	STEM/EDS MICROGRAPHS AND LINE SCANS SHOWING EFFECT OF HEAT TREATMENT CONDISTSIONS & MICROSTRUCTURE	77

TABLE OF FIGURES

2.0 LITERATURE REVIEW.....3

Figure 2.1 Typical appearance of intermetallic particles observed in the Cu-rich AA7075 alloy in the (A) T6 condition, and (B) solution heat-treated condition4

Figure 2.2 Typical appearance of the intermetallic particles observed in the Cu-lean AA7003 alloy.....4

Figure 2.3 TEM micrograph showing the typical appearance of dispersoids in the Cu-lean (a) Al-4.7% Zn-2.8% Mg (b) Al-4.38% Zn-2.97% Mg experimental alloys6

Figure 2.4 TEM micrograph showing the typical appearance of (a) Al₃Zr and (b) Al₁₈Mg₃Cr₂ dispersoids in the Cu-rich AA7075 alloy (solution-treated condition)7

Figure 2.5 TEM micrographs showing the typically appearance of η (MgZ₂ type) precipitates in the grain boundary region in the (A) Cu-lean AA7004-T6 alloy and (B) Cu-rich AA7039-T6 alloy.....9

Figure 2.6 SEM micrograph showing typical appearance of the τ (Mg₃Zn₃Al₂) precipitates observed in an Al-6% Zn- 2.2% Mg alloy9

Figure 2.7 Plot showing the variation in the composition of the Mg(Zn,Cu,Al)₂ grain boundary precipitates, as a function of alloy Cu content11

Figure 2.8 SEM micrograph of the peripheral pitting around an Al₇Cu₂Fe intermetallic particle found in an AA7075-T651 sample anodically polarized to to -750mV_{SCE} in.....14

0.1 M NaCl solution at pH 6 for 10 h [57].14

Figure 2.9 Optical micrograph showing typical appearance of the surface of (a) Cu-lean AA7004-T6, and (b) Cu-rich AA7075-T6 after anodic polarizing to 1 mA/cm² in deaerated 0.5 M NaCl at pH 3.56.....15

4.0 EXPERIMENTAL DETAILS.....25

Figure 4.1 Photograph of the extruded bumper beam cut in cross-section, showing the general structure, major dimensions and orientation axis.25

5.0 RESULTS.....35

Figure 5.1 Microstructure of the three orthogonal sections of the AA7003 extrusion in the (a) naturally-aged T4 heat-treated (as-received) condition, (b) artificially-aged T6 heat-treated condition, and (c) artificially-aged paint bake heat-treated condition. Magnified view of the ST-LT microstructure in the T4 heat-treated condition (d).....36

Figure 5.2 Bar charts showing influence of the heat-treated condition on the AA7003 extrusion grain size distribution of the (a) LT-ST cross-section microstructure, and (b) L-ST cross-section microstructure.....37

Figure 5.3 Bar charts showing influence of the heat-treated condition on the AA7003 extrusion grain aspect ratio of the (a) LT-ST cross-section microstructure, and (b) L-ST cross-section microstructure38

Figure 5.4 Typical appearance and elemental composition of the randomly-distributed, micro-sized irregular-shape second phase particles found on the surface (L-LT plane) microstructure of the AA7003 extrusion in the (a) naturally-aged T4 heat-treated (as-received) condition, (b) artificially-aged T6 heat-treated condition, and (c) artificially-aged paint bake (PB) condition.39

Figure 5.5 Typical appearance and elemental composition of the randomly-distributed, micro-sized rectangular-shape second phase particles found on the surface (L-LT plane) microstructure of the AA7003 extrusion in the (a) naturally-aged T4 heat-treated (as-received) condition, (b) artificially-aged T6 heat-treated condition, and (c) artificially-aged PB condition.40

Figure 5.6 STEM micrographs of the grain boundary regions in the coarse, recrystallized surface layer and the fibrous, non-recrystallized interior for the naturally-aged T4, artificially-aged T6 and artificially-aged paint bake (PB) heat-treated conditions.....43

Figure 5.7 Potentiodynamic polarization curves for AA7003 extrusion with the three heat-treated conditions in deaerated 0.5 M NaCl solution with a pH 3.56 with (a) coarse, recrystallized (L-LT) surface layer exposed to the solution, and (b) fibrous, non-recrystallized (L-LT) interior exposed to the solution.45

Figure 5.8 Photographs of the exposed surface of the AA7003 extrusion electrodes in the three heat-treated conditions after exposure potentiodynamic anodic polarization to a current density of 1 mA/cm² in deaerated 0.5 M NaCl solution with a pH 3.56 at room temperature.46

Figure 5.9 Bar chart comparing the influence of heat-treated condition and propagation direction on the maximum depth of attack observed in AA7003 extrusion after exposure to the ASTM G110 test solution (57 g NaCl and 10 ml of H₂O₂ diluted with H₂O to 1000 mL) for 24 h at 30°C.48

Figure 5.10 Cross-section (LT-ST) micrographs of the AA7003 extrusion coupon in the three heat-treated conditions, with the maximum depth of attack after exposure to the ASTM G110 test solution (57 g NaCl and 10 ml of H ₂ O ₂ diluted with H ₂ O to 1000 mL) for 24 h at 30°C.....	49
Figure 5.11 Photographs of the triplicate sets of the AA7003 extrusion coupons in the (a) naturally-aged T4 condition, (b) artificially-aged T6 condition, and (c) artificially-aged PB condition, immediately after exposure to ASTM G34 test solution (468 g NaCl, 100 g KNO ₃ and 12.6 mL 70 wt.%-HNO ₃ diluted in distilled H ₂ O to 2000 mL) at room temperature for 48 h	51
Figure 5.12 Bar chart comparing the influence of heat-treated condition on the maximum depth of attack observed in AA7003 extrusion after exposure to the ASTM G34 test solution (468 g NaCl, 100 g KNO ₃ and 12.6 mL 70 wt.%-HNO ₃ diluted in distilled H ₂ O to 2000 mL) at room temperature for 48 h	52
Figure 5.13 Cross-section (L-ST) micrographs of the AA7003 extrusion coupon in the (a) naturally-aged T4 condition, (b) artificially-aged T6 condition, and (c) artificially-aged PB condition, with the maximum depth of attack after exposure to ASTM G34 test solution (468 g NaCl, 100 g KNO ₃ and 12.6 mL 70 wt.%-HNO ₃ diluted in distilled H ₂ O to 2000 mL) at room temperature for 48 h	53
6.0 DISCUSSION.....	54
Figure 6.1 Intergranular corrosion propagation mechanism.....	63
Figure 6.2 Galvanic couple formation in naturally-aged T4 and artificially-aged T6 heat treated condition.....	64
APPENDIX.....	77
Figure 1 STEM/EDS scans for naturally aged as-received T4 courser grain microstructure	77
Figure 2 STEM/EDS scans for naturally aged as-received T4 finer grain microstructure	78
Figure 3 STEM/EDS scans for simulated paint bake PB courser grain microstructure....	79
Figure 4 STEM/EDS scans for simulated paint bake PB finer grain microstructure.....	80
Figure 5 STEM/EDS scans for artificially aged T6 courser grain microstructure.....	81
Figure 6 STEM/EDS scans for artificially aged T6 finer grain microstructure.....	82

1.0 INTRODUCTION

Bumper assemblies play a predominant role in the passive safety of an automobile, since they are one of the main structures for absorbing the collision energy in the event of an automobile crash. Heat-treatable Aluminum Association (AA) 6XXX-series (Al-Mg-Si) and AA7XXX-series (Al-Zn-Mg) alloy extrusions, with relatively high strength, toughness, energy absorption, weldability, and formability, make it possible to design cost-competitive bumper systems to crush in a controlled fashion [1-5]. Moreover, the weight savings attained using aluminum alloys in this application help with improving fuel efficiency and reducing harmful emissions [6,7].

Bumper systems have changed drastically over the last 20 to 30 years, and they continue to change as automakers adjust to new regulations, strive to improve safety, make vehicles more fuel efficient, and reduce manufacturing costs. Both the aluminum alloy and automotive industries, working together, are developing new ways to use the advanced high-strength aluminum alloys available today with superior strength and formability characteristics. In this context, Cu-lean AA7XXX extrusions, which exhibit higher strength than AA6XXX extrusion, represent an attractive material from which to fabricate bumper assemblies [2-5].

However, a major technological issue preventing widespread utilization of Cu-Lean AA7XXX extrusions for bumper assemblies is the susceptibility to intergranular corrosion modes (including exfoliation and stress corrosion cracking), particularly when (fusion) welded [1]. The susceptibility to intergranular corrosion modes of Cu-rich AA7XXX alloys, such as AA7075-T6, has been studied and reviewed in great detail because of the widespread utilization of such alloys in the aerospace industry [8-10].

Intergranular corrosion damage accumulation is predominantly observed in the grain boundary region, with the susceptibility being directly relatable to the development of local anodes and cathodes across the grain boundary regions. However, the controlling microstructure parameters are still under debate [11-14].

Although studies have addressed the role played by the alloyed copper on the susceptibility of AA7XXX alloys to intergranular modes of corrosion, the focus has been placed on susceptibility as a function of the Cu content rather than a between Cu-lean and Cu-rich alloys. Therefore, the role of microstructure on the susceptibility to intergranular corrosion damage of Cu-lean AA7XXX-series is much less understood [15]. A better understanding of the controlling microstructure factors needs to be attained to greatly enhance the engineering development stages by allowing analysis models to better predict the structural performance behaviour of welded Cu-lean AA7XXX alloys.

A study was undertaken to achieve a better understanding of the controlling microstructure factors involved in the intergranular corrosion and exfoliation corrosion of Cu-lean AA7003 alloy extrusions, as a function of the heat-treated condition. The heat treatments of interest include the naturally aged T4 condition, representing the as-extruded condition, an artificially-aged T6 condition, representing a post weld stress relief heat-treated condition, and an artificially aged paint-bake heat-treated condition.

2.0 LITERATURE REVIEW

2.1 ALLOY MICROSTRUCTURE

The microstructure of AA7XXX Al alloys is heterogeneous and contains the solid solution Al matrix and three types of second phase particles, namely coarse inter-metallic particles, coarse dispersoid particles and fine strengthening precipitate particles [16]. The classification of these second phase particles has been on the role played by each with respect to the mechanical properties and corrosion properties of the alloy [17]. A more detailed discussion of the role played with respect to the corrosion properties is provided separately below.

2.1.1 INTERMETALLICS

Intermetallic particles, also known as constituent particles, are generally large irregular shaped and vary in size between 1-10 microns (μm). These second phase particles are formed by interaction between the alloying elements (Al, Zn, Mg, Cu) and impurities present during solidification (Fe, Mn, Si), which remain undissolved in subsequent thermomechanical processing. Impurities like Fe and Si tend to form a cell or dendrite arm boundary during the solidification process due to their low solubility [7,16,18]. At these sites, impurities then react with the alloying elements (Zn, Mg, Cu) to form the intermetallic particles.

Typically, intermetallic particles are not uniformly distributed within the alloy, and can form clusters of high density particles, due to higher Fe and Si contents [19]. Rolling or extrusion can break these intermetallic particles, and align them into bands

along the working (rolling/extrusion) direction. In Cu-rich AA7xxx alloys like AA7075 and AA7475, $\text{Al}_7\text{Cu}_2\text{Fe}$, Mg_2Si , Al_3Fe , Al_2CuMg , $\text{Al}_{12}(\text{Fe,Mn})_3\text{Si}$, $\text{Al}_{40}\text{Cu}_{15}\text{Mg}_{25}\text{Zn}_{20}$, $(\text{Al,Cu})_6(\text{Fe,Cu})$ or $\text{Al}_{23}\text{CuFe}_4$ intermetallics have been observed [16,20-24]. Figure 2.1 shows the typical appearance of intermetallic particles in the Cu-rich AA7075 alloy in the T6 and solution heat-treated conditions [23].

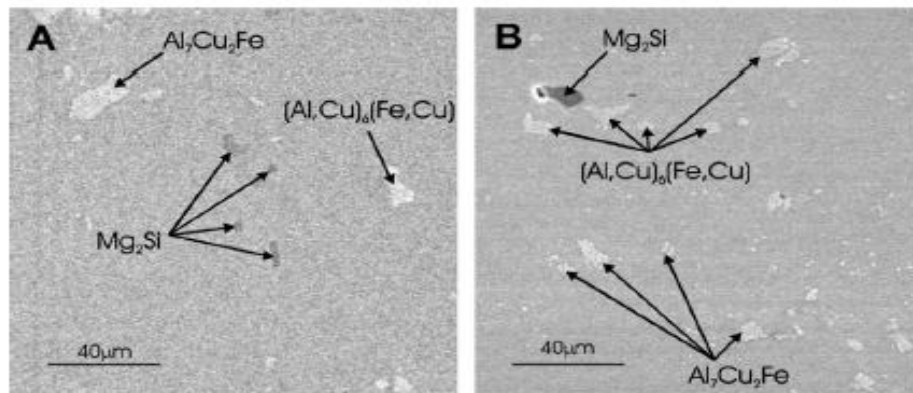


Figure 2.1 Typical appearance of intermetallic particles observed in the Cu-rich AA7075 alloy in the (A) T6 condition, and (B) solution heat-treated condition [23].

In the Cu-lean AA7003 alloy, Mg_2Si and $\text{Al}(\text{Fe,Mn})\text{SiZn}_4$ intermetallics have been observed, as shown in Figure 2.2 [25]. Interestingly, no Cu-bearing intermetallic particles were observed in this alloy.

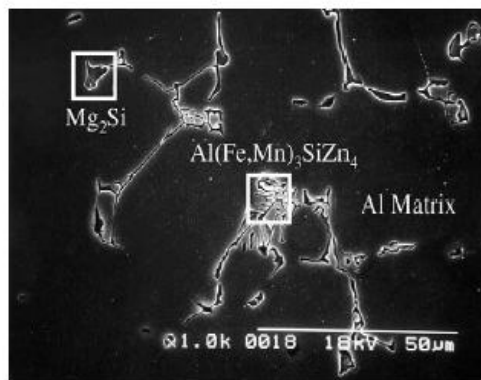


Figure 2.2 Typical appearance of the intermetallic particles observed in the Cu-lean AA7003 alloy [25].

The Cu-rich intermetallic particles are generally insoluble during the typical solution heat treatment and subsequent aging processes applied to Cu-rich AA7XXX alloys [7,26]. This is because of the low solubility of Fe in Al, which is further reduced by presence of other alloying elements. This can be observed in the Cu-rich AA7075, AA7475 and AA7010 alloys, where the Cu- and Fe-rich intermetallic particles remain unchanged by solution heat treatment and different temper conditions [21]. Although Si-rich intermetallic particles can be dissolved during a homogenization treatment, they do not completely dissolve during practical homogenization treatments [27]. If the solution heat treatment is performed at higher temperatures, say around 480°C, the other types of intermetallic particles containing Cu, Mg, and Zn could be dissolved, but this is not practiced in order avoid local melting within the alloy [20].

2.1.2 DISPERSOIDS

Dispersoid particles are comprised of alloying elements that are highly insoluble in Al. They are formed at high temperatures during the homogenization treatment by the reaction of additives like Cr, Mn and Zr with alloying elements. Their size is comparatively smaller than intermetallic particles, and ranges from 0.05 µm to 0.5 µm. Typical dispersoid particles observed in AA7XXX alloys include Al_3Ti , Al_6Mn , Al_3Zr and $\text{Al}_{20}\text{Cu}_2\text{Mn}_3$ [16, 28, 29, 30]. For the Cu-rich AA7055 and AA7050 (Zr-containing) alloys, dispersoid particles having the composition of Al_3Zr have been observed [30-32], whereas in AA7075 and AA7475 (Cr-containing) alloys, dispersoid particles having the composition of $\text{Al}_{18}\text{Mg}_3\text{Cr}_2$ have been observed [31].

Dispersoids control the grain size, degree of recrystallization of the alloy and quench sensitivity of the alloy (extent to which slower cooler rates can be tolerated such that there is no precipitation during cooling). It is found that Zr-containing alloys have lower quench sensitivity than Cr containing alloys [33]. With the exception of Mn, most of the elements present in dispersoids corrode in a passive state when in contact with an aqueous solution. These dispersoids are randomly distributed in the microstructure since they precipitate directly from the as-cast microstructure. This is a characteristic of the heterogeneous distribution of elements forming them [30]. Unlike intermetallic particles, dispersoid particles have been observed to slightly change composition during subsequent heat treatments. For example, overaging of the Cu-rich AA7075 alloys has been found to decrease the Zn content and increase the Al content of $\text{Al}_{18}\text{Mg}_3\text{Cr}_2$ dispersoid particles [21]. Surprisingly, the effect on the change in composition on the corrosion behaviour has not been studied in much detail [21]. The typical appearance of dispersoid particles, as observed in the Cu-lean experimental Al-Zn-Mg alloys [34] and in the Cu-rich AA7075 alloy [21], is shown in Figures 2.3 and 2.4 respectively.

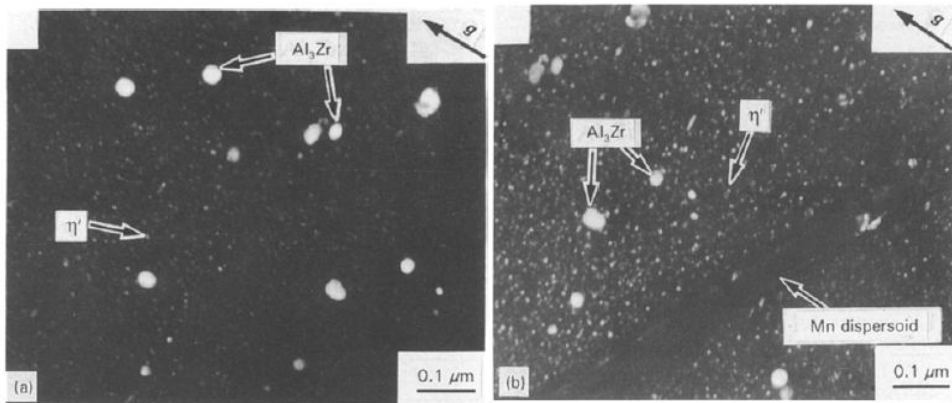


Figure 2.3 TEM micrograph showing the typical appearance of dispersoids in the Cu-lean
 (a) Al-4.7% Zn-2.8% Mg (b) Al-4.38% Zn-2.97% Mg experimental alloys [34].

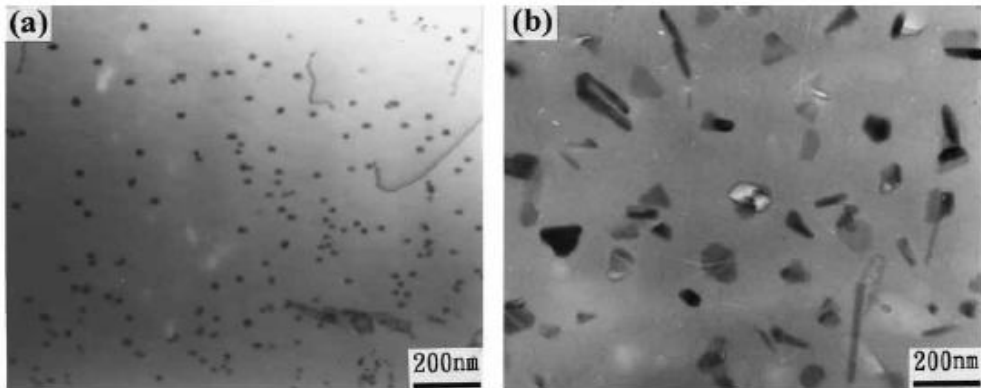
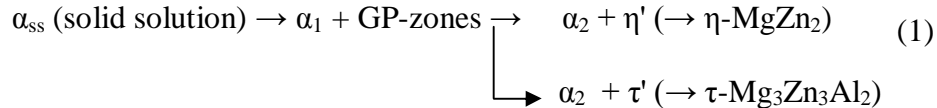


Figure 2.4 TEM micrograph showing the typical appearance of (a) Al_3Zr and (b) $\text{Al}_{18}\text{Mg}_3\text{Cr}_2$ dispersoids in the Cu-rich AA7075 alloy (solution-treated condition) [21].

2.1.3 STRENGTHENING PARTICLES

The high strength of the AA7XXX alloys in the hardened state is typically due to the fine distribution of precipitates, the η' or τ' metastable phases in particular, which are produced by artificial aging of the supersaturated solid solution (T6 temper). The precipitation process is often represented by the simplified sequence [35-41]:



Strengthening precipitates are formed by precipitation during aging of high strength aluminum alloys. They range in size from 1 nm to 100 nm and have spherical, lath, needle, plate like or different shape [16,42-44]. Generally, there are three phases of a given strengthening precipitate observed, namely GP zones, metastable precipitates and equilibrium precipitates [35-46]. In GP zones, solute atoms are present as fine clusters, which has same crystal structure with the matrix. Metastable precipitates have either coherent or partially coherent crystal structure with the matrix. Equilibrium precipitates are largest in size of all three and are completely incoherent with the matrix structure.

The high strength of AA7XXX aluminum alloys is typically derived from the presence of GP zone and metastable precipitates [42,47].

It is generally accepted that GP zones nucleate either homogeneously in the matrix or heterogeneously at vacancies or dislocation clusters. Transformation of GP zones or heterogeneous nucleation leads to the formation of the metastable precipitates and subsequent transformation of these precipitates leads to formation of the equilibrium precipitates. Equilibrium phases can also be formed by heterogeneous nucleation at dislocations, grain boundaries or at dispersoid-matrix interfaces [39]. Solution heat treatment produces a large amount of segregation of solute atoms, Mg and Zn at grain boundaries [47, 48]. During aging, solute atoms present in solid solution are depleted due to precipitation of strengthening particles in both matrix and on grain boundaries [35-41], as in sequence (1).

The grain boundary precipitates in AA7XXX alloys has been examined in detail using TEM, coupled with EDS. The typical appearance of such precipitates, as observed in the AA7004 (0.013 wt.% Cu) and AA7039 (0.077 wt.% Cu) alloys in solution heat treated and artificially aged T6 heat treatment condition, is shown in Figure 2.5 [15]. The TEM micrographs clearly show the presence of fine hardening precipitates in both the Al matrix and coarse rod-shaped hardening precipitates on the grain in both alloys. The composition of Al-rich SDZ (region adjacent to grain boundary with lesser/no precipitation) was measured to be essentially the same for both alloys, namely Al-2(wt.%)Mg. In contrast, the composition of the (η phase) grain boundary precipitates were found to be different, namely generic $Mg(Zn,Cu,Al)_2$ in the Cu-rich AA7039 alloy and $MgZn_2$ in the Cu-lean AA7004 alloy. Although rarely reported, precipitates of the τ

phase ($Mg_3Zn_3Al_2$) in Al-6% Zn- 2.2% Mg alloy has been reported [48]. Figure 2.6 shows the typical appearance of this precipitate.

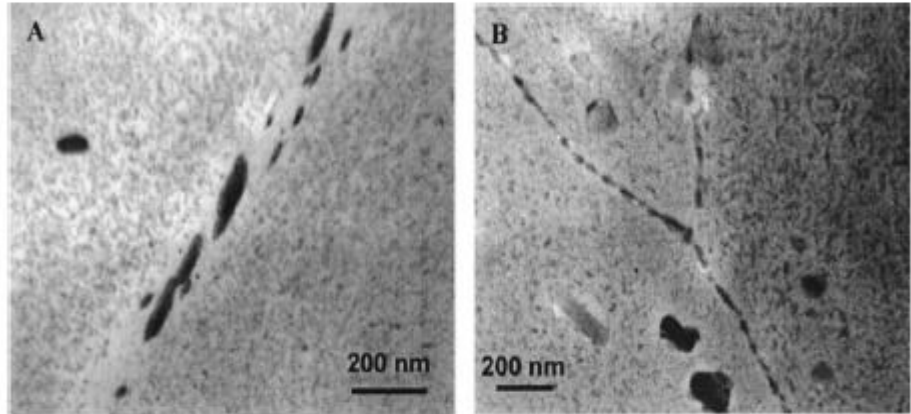


Figure 2.5 TEM micrographs showing the typically appearance of η ($MgZn_2$ type) precipitates in the grain boundary region in the (A) Cu-lean AA7004-T6 alloy and (B) Cu-rich AA7039-T6 alloy [15].

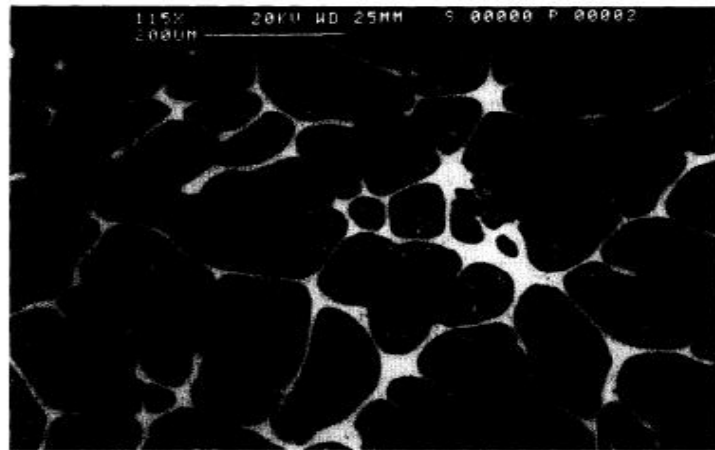


Figure 2.6 SEM micrograph showing typical appearance of the τ ($Mg_3Zn_3Al_2$) precipitates observed in an Al-6% Zn- 2.2% Mg alloy [48].

The composition of GP zones and η' (metastable) phase have a typically lower Zn/Mg ratio than in the η (equilibrium) phase, and is dependent on the alloy composition and heat treatment applied [36,38,49,50]. For the peak strength tempers (T6 and T651) of the Cu-rich AA7075 alloy, η' precipitates are observed to be distributed in the matrix,

whereas η precipitates are found to be distributed on the grain boundaries. For the over-aged temper (T73) of the Cu-rich AA7075 alloy, η precipitates are observed to be distributed in Al matrix and on the grain boundaries, whereas η' precipitates are found to be present only in small quantities, depending on degree of overaging [42-46].

Alloyed Cu has been found to have a strong influence on composition of the grain boundary regions in AA7XXX alloys. For example, the solubility of Cu in the η ($MgZn_2$) precipitates was studied in the AA7150 alloy, and was found to depend on the heat-treated condition, T6 verse T7 [14]. For the analysis of the EDS data, it was assumed that (i) the generic composition of the grain boundary precipitates is $Mg(Zn,Cu,Al)_2$ with the extreme composition being $CuAlMg$, (ii) the Mg content in η phase is fixed at 33.33%, and (iii) the SDZ has a composition of Al-2(wt.%)Mg. The following equation was used to calculate the composition of the grain boundary precipitates [14]:

$$(C_i)_{mppt} = V_{SDZ} \times (C_i)_{SDZ} + V_{ppt} \times (C_i)_{ppt} \quad (2)$$

where, C_i is the composition of i^{th} element (Mg, Zn, Cu, Al) in atom%, $(C_i)_{mppt}$ is the measured composition of precipitate in atom%, $(C_i)_{SDZ}$ is composition of SDZ, $(C_i)_{ppt}$ is calculated actual composition of precipitate in atom%, V_{SDZ} and V_{ppt} are volume fractions of X-ray excitation volume obtained during analysis of precipitate of SDZ and precipitate, respectively. Using the aforementioned assumptions and Equation (2), it was found that the T7 condition contained more Cu in the precipitates (matrix and grain boundary) than the T6 condition, whereas the composition of the SDZ remained unaltered.

The same procedure for calculating variations in the Cu content across the grain boundary region was used for AA7004, AA7039, AA7029, AA7050 and AA7075 alloys

in the T6 condition [15]. It was found that the Cu content in the generic $Mg(Zn,Cu,Al)_2$ grain boundary precipitates increased with the Cu content in the alloy, whereas the Zn content in the $Mg(Zn,Cu,Al)_2$ precipitate decreased and the Al content remains the same. The variation in the composition of the $Mg(Zn,Cu,Al)_2$ precipitate with the alloy Cu content is shown in Figure 2.7 [15].

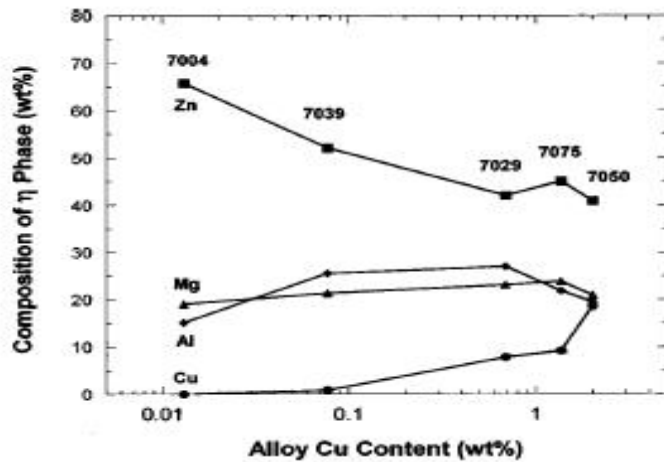


Figure 2.7 Plot showing the variation in the composition of the $Mg(Zn,Cu,Al)_2$ grain boundary precipitates, as a function of alloy Cu content [15].

2.2 SECOND PHASE ELECTROCHEMICAL REACTIVITY

The second phase particles have a different composition than the Al matrix, thus the electrochemical behavior of these particles is significantly different from the Al matrix. It is noted here that SEM/EDS studies have revealed that partial substitution of alloying elements within the second phase particles can occur [15, 16], which can affect the resultant electrochemical reactivity of the Al matrix and the second phase particles.

Two characteristic electrochemical potentials are readily quoted when discussing the corrosion behaviour of AA7XXX alloys, namely the corrosion potential (E_{corr}) and the breakdown potential (E_b). The corrosion potential is defined as the potential of the corroding surface in an electrolyte, with respect to reference electrode, established under

an open circuit conditions [51]. In contrast, the breakdown potential is defined as the least noble potential at which the local breakdown of passive film occurs on the Al alloy surface [23]. Typical magnitudes for these characteristic potentials can be obtained from an anodic polarization curve measured in the service environment of interest.

It has been repeatedly found that noble second phase particles, whose corrosion potentials are greater than that of the AA7XXX alloy, greatly influences the corrosion behavior of Al matrix. In contrast, active second phase particles, whose corrosion potentials are less than that of the AA7XXX alloy, do not have any impact on corrosion behaviour of the Al matrix. For example, at the corrosion potential for the Cu-rich AA7075 alloy in 0.1 M NaCl at room temperature, it was observed that Mg₂Si and MgZn₂ particles experienced severe anodic dissolution [16]. In contrast, at an anodic polarized potential above the breakdown potential of the alloy, corresponding to the corrosion potentials of the Al₃Fe and Al₂Cu second phase particles, the Al matrix experienced serve anodic dissolution [16]. Table 2.1 tabulates the corrosion potential and the breakdown potential observed for a selection of second phase particles present in AA7XXX alloys [16].

Table 2.1 Corrosion Potential of Intermetallic Phases [16]

Phase Present	Corrosion Potential (mV _{SCE} in 0.1M NaCl)	Breakdown Potential (mV _{SCE} in 0.1M NaCl)
MgZn ₂	-1029	Not Observed
Al ₇ Cu ₂ Fe	-551	-448
Mg ₂ Si	-1538	Not Observed
Al ₃₂ Zn ₄₉	-1063	Not Observed
Al ₂ CuMg	-943	80
Al ₃ Fe	-539	106
Al ₂ Cu	-665	-544
Al	-823	-610

2.3 CORROSION PROPERTIES OF AA7XXX ALLOYS

Generally corrosion modes of Al alloys are classified into two categories, namely structure-dependent and local chemistry of the environment-dependent. Intergranular corrosion, exfoliation corrosion and stress corrosion cracking fall under the category of structure-dependent corrosion, and are greatly influenced by the metallurgical condition. Uniform and pitting corrosion fall into the latter category. One of the important localized forms of corrosion is pitting corrosion, as it can develop into intergranular corrosion, thereby leading to exfoliation corrosion and stress corrosion cracking [52].

2.3.1 PITTING CORROSION

Pitting corrosion can be defined as electrochemical phenomena resulting in removal of metal (or breaking of naturally formed surface oxide) at localized sites by formation of cavities by anions like Cl^- in the given electrolyte [51,53]. Pitting corrosion in Al alloys is due to the differences in electrochemical potential within the heterogeneous microstructure, which consists of intermetallic particles, dispersoid particles, matrix and grain boundary strengthening precipitates and solute depleted zone (SDZ) adjacent to the grain boundaries. Pitting corrosion occurs only above a characteristic breakdown potential known as the pitting potential, which is unique for every alloy in a given electrolyte. A critical factor is the local alkalinization of solution that is caused by cathodic reactions occurring on the surface of second phase particles, intermetallic particles in particular. Hydroxyl ions are generated by oxygen or water reduction on the surface of an intermetallic particle, which then causes chemical attack of protective oxide layer on the Al matrix at the periphery of the intermetallic particle [16,54,55].

In Cu-rich AA7075 and AA7050 alloys, $\text{Al}_7\text{Cu}_2\text{Fe}$ and $(\text{Al},\text{Cu})_6(\text{Fe},\text{Cu})$ intermetallic particles act as cathodic sites, causing significant dissolution of surrounding anodic Al matrix [56, 57]. Size of the intermetallics is smaller than the matrix, and so the ratio of cathode to anode area is small. Hence, the rate of Al matrix dissolution at the periphery of the intermetallic particle increases with the size (surface area) of the intermetallic particle. Generally the area of localized attack surrounding the intermetallic is five times the size of intermetallic (of about 100 μm) [16]. Cathodic intermetallics are often present as clusters, therefore attack at an intermetallic cluster can expose a large area of the Al matrix and produce severe pitting [55-57]. Figure 2.8 shows an SEM image of an $\text{Al}_7\text{Cu}_2\text{Fe}$ particle, followed cross-sectioning with a focused ion beam, found in an AA7075-T651 sample after anodic polarization to -750mV_{SCE} in 0.1 M NaCl solution at pH 6 for 10 h, which clearly shows peripheral pitting damage [57].

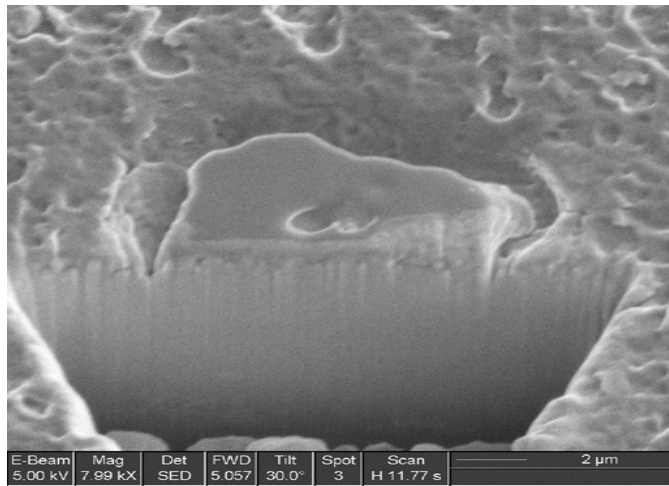


Figure 2.8 SEM micrograph of the peripheral pitting around an $\text{Al}_7\text{Cu}_2\text{Fe}$ intermetallic particle found in an AA7075-T651 sample anodically polarized to -750mV_{SCE} in 0.1 M NaCl solution at pH 6 for 10 h [57].

The influence of the alloy Cu content on the corrosion behaviour of AA7XXX alloys has been studied in some detail [15]. One breakdown potential was observed for the Cu-lean AA7004 alloy, whereas two breakdown potential were observed for the Cu-rich AA7039, AA7075, AA7050 and AA7029 alloys. The single breakdown potential for AA7004 was found to be associated with pitting corrosion, whereas the more noble of the two breakdown potentials for the remaining AA7XXX alloys under study was found to be associated with pitting and intergranular corrosion. The more active breakdown potential was attributed to the transient dissolution of fine Cu-containing hardened precipitates. Figure 2.9 shows presence of pits on the surface of the Cu-lean AA7004 and the Cu-rich AA7039 sample after anodic polarization to 1 mA/cm^2 in 0.5 M NaCl at pH 3.56. [15].

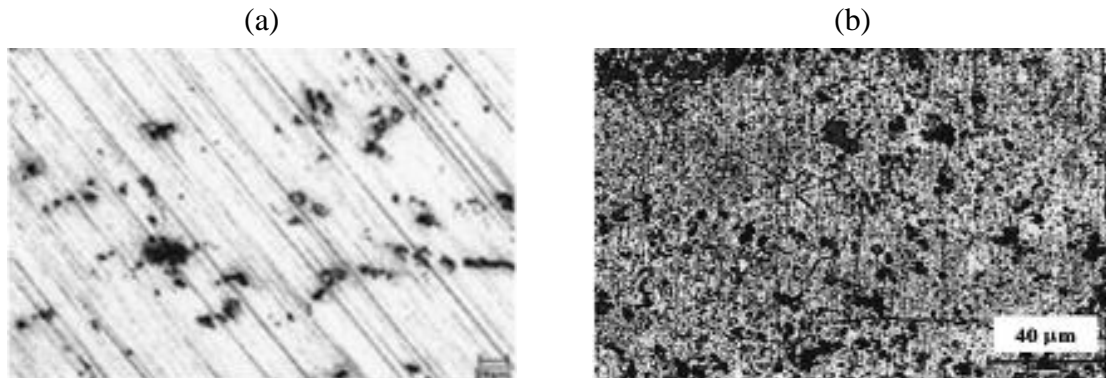


Figure 2.9 Optical micrograph showing typical appearance of the surface of (a) Cu-lean AA7004-T6, and (b) Cu-rich AA7075-T6 after anodic polarizing to 1 mA/cm^2 in deaerated 0.5 M NaCl at pH 3.56 [15].

2.3.2 INTERGRANULAR CORROSION

Intergranular corrosion can be defined as selective attack of the grain boundary or adjacent regions without much attack on the grains [51,53]. Formation of precipitates on the grain boundaries, due to an applied heat treatment, can increase the susceptibility of

AA7XXX alloys to intergranular corrosion. Intergranular corrosion is also known to cause exfoliation corrosion, as a result of the internal stress at the grain boundaries caused by the formation of corrosion products. In general, the susceptibility of AA7XXX alloys to intergranular corrosion and exfoliation corrosion is due in large part to the formation of a SDZ, segregation of solute atoms at grain boundaries and precipitation of strengthening particles on grain boundaries. Galvanic couple theory, anodic dissolution of grain boundary precipitates and the SDZ breakdown model are three major proposed mechanisms of intergranular corrosion [58].

The first theory proposed is the galvanic couple theory. According to this theory, susceptibility to intergranular corrosion is due to the differences in the corrosion potential of the anodic grain-boundary constituents (SDZ and/or precipitates) and the Al matrix, which leads to localized galvanic corrosion [59]. This theory was proposed to explain observations made in Al-Cu alloys. It was found that, for Al-Cu alloys in the peak-aged condition, the grain boundaries were 200 mV more active than the grain interiors due to the Cu-depleted zone along the grain boundaries. In the over-aged condition, there was no difference between the grain boundary and the grains due to precipitation of CuAl_2 in the matrix. It was concluded that the susceptibility of the peak aged temper to intergranular corrosion was due to the difference in corrosion potentials of the grain boundary and the grain interiors. This theory has also been used to explain the intergranular corrosion of Cu-rich AA7XXX alloys [58]. However, many experiments have shown that intergranular corrosion is not observed if the solutions do not contain chloride (Cl^-) anions [60]. Thus, this theory fails to explain the role of aggressive anions in intergranular corrosion mechanism.

The SDZ breakdown model was also proposed based on experiments performed using Al-Cu alloys. According to this theory, intergranular corrosion arises due to difference in breakdown potential between Al matrix grain and SDZ adjacent to grain boundary [60]. It was found that the Al-4at%Cu alloy, in the peak-aged condition, exhibited two breakdown potentials when polarized in chloride solution. The more active breakdown was associated with intergranular corrosion and the noble breakdown was associated with both pitting corrosion in the matrix and intergranular corrosion. In the over-aged condition, only one breakdown potential was observed, and was associated with pitting corrosion in the matrix. In the peak-aged condition, the grain boundary of the alloy was depleted in Cu due to precipitation of CuAl_2 at the grain boundary. This resulted in the breakdown potential of the SDZ being more active than that of the Al matrix grain. In contrast, in the over-aged condition, precipitation of CuAl_2 within the Al matrix grain lowered the breakdown potential of the matrix such that it was similar to that of the grain boundary. This similarity in breakdown potential was argued as the reason for the reduced susceptibility of the over-aged condition to intergranular corrosion.

A third mechanism was proposed to explain the intergranular corrosion of Al-Li-Cu alloys and involves the dissolution of the T_1 grain-boundary precipitate phase [61]. According to this theory, the dissolution of the T_1 grain-boundary phase results in the creation of an aggressive occluded environment, which leads to the dissolution of the grain boundary and continuous grain boundary attack.

Two critical factors associated with intergranular corrosion of AA7XXX alloys of particular interest include the influence of the heat treated condition and of the alloyed Cu content. The degree to which the heat-treated condition affects the susceptibility has been

related to the number of breakdown potentials observed in the anodic polarization behaviour [11, 62, 63]. For example [11, 63], the anodic polarization curve of AA7XXX alloys in deareated NaCl solution for the W (Wrought) condition showed only one breakdown potential, which corresponded to pitting corrosion in the single-phase solid solution matrix. In contrast, the alloys were susceptible to intergranular corrosion and exhibited two breakdown potentials in the artificially aged T6 condition. The noble breakdown potential corresponded to the pitting of solid solution matrix (containing less Zn and Mg), whereas the active breakdown potential corresponded to the pitting of the solute-enriched grain boundary region. The T7 condition was found to exhibit decreased susceptibility to intergranular corrosion and the polarization curve consisted of a single breakdown potential, which corresponded to pitting corrosion. It was argued that, in the T7 condition, Cu is removed from solid solution and incorporated in $Mg(Zn,Cu,Al)_2$ grain boundary precipitates resulting in the shift of second breakdown potential to negative value while the solute enriched grain boundary region becomes narrower and less continuous.

The influence of the alloy Cu content on the localized corrosion behaviour in acidified, deaerated NaCl was studied using a series of AA7XXX alloys in the T6 heat-treated condition [15]. Two breakdown potentials were observed for all alloys except for the Cu-lean (0.013 wt.% Cu) AA7004, and both were found to increase logarithmically with alloy Cu content. The first breakdown potential (absent in AA7004) corresponded to Cu-content controlled transient dissolution associated with attack of the fine hardening particles and the surrounding solid solution in a thin surface layer. The second breakdown potential was associated with combined intergranular corrosion and selective grain attack,

and was argued to be controlled by the Cu content in the matrix, including the hardening particles.

2.3.3 EXFOLIATION CORROSION

Exfoliation corrosion is a form of intergranular corrosion that occurs on the surface of wrought Al alloys with elongated grain structure. The internal stress caused by voluminous corrosion products forces the layer of uncorroded metal surface away from the body of the material, thereby giving rise to a layered appearance [51,53]. Exfoliation corrosion is intergranular in nature due to galvanic interaction between grain boundary and the adjacent SDZ [64]. In general, for a highly directional microstructure, a corrosive environment and preferential anodic path along the grain boundaries, there exists three important driving factors for EFC to occur [51], which are described in some detail below.

It is generally accepted that the corrosion product of Al alloys is hydrated alumina, Al(OH)_3 . During localized corrosion in Cl^- -containing environments, Al ions (Al^{3+}) are hydrolyzed as represented in following sequence (3):



The hydrated alumina gel formed is not stable and crystallizes with time to boehmite or bayerite or hydrargilite [68]. The volume of hydrated alumina is larger than the matrix that converts it to corrosion product. Hence, a larger amount of stress exerted by these corrosion products at intergranular corrosion sites lifts the surface grains promoting exfoliation corrosion [65,66]. The measurement of corrosion product force for

Cu-rich AA7150, AA7055 and AA7449 alloys in the peak-aged condition have revealed a dependence of grain aspect ratio on the stress generated by the corrosion product [66].

The mechanism of exfoliation was studied in Al-5%Zn-1%Mg alloy [67]. In the naturally-aged condition, GP zones were found to be the main phase present. In this condition, exfoliation corrosion is believed to be caused by local galvanic corrosion activity between the noble Al matrix grain and the α -Al(Fe,Mn)Si particles aligned along the extrusion direction and the narrow zone of active Mg,Zn-rich precipitates (anode). This anodic zone is attacked leading to exfoliation along the boundaries. In this context, the Al matrix is cathodically protected, since it is depleted in Zn and Mg, whereas the active MgZn₂ precipitates are subjected to anodic dissolution. In the artificially-aged condition, it was observed that the MgZn₂ precipitates were evenly distributed throughout the Al matrix, thereby causing the corrosion to be more general in nature rather than exfoliation corrosion. These concepts were reinforced by anodic polarization measurements of the various phases corresponding to the naturally-aged and artificially-aged conditions, which showed that the phases in the artificially-aged condition were more noble.

Important factors that influence exfoliation corrosion include alloy composition, grain aspect ratio, heat treatment and service environmental conditions. Exfoliation corrosion was studied in the Al-5%Zn-1%Mg alloy [67]. In this study, it was found that the Al matrix contained cathodic α -Al(Fe,Mn)Si particles. As the Fe and Mn contents were increased, so to was the amount of the cathodic α -Al(Fe,Mn)Si phase, which tended to increase the susceptibility to exfoliation corrosion. It was suggested that the same effect might occur for increasing Si and Cr content. Moreover, it was suggested that the

role of Mg and Zn in the exfoliation path is secondary, since both diffuse readily at normal homogenizing temperatures. In contrast, Mn, Fe and Zr play an important role, since they diffuse slowly and maintain stable concentration [68, 69]. However, for the Cu-lean AA7004 alloy, which contains both Fe and Mn, it was found that the susceptibility to exfoliation corrosion is higher and the corrosion path is depletion of Mn at grain boundaries [9, 70]. It was proposed that an electrochemical cell consisting of Mn-rich and Mn-depleted regions arises, which results in exfoliation path as Mn, when replaced by Fe in α -AlFeSi, results in depletion of Mn from surrounding regions.

One of the most important factors for exfoliation corrosion is the elongated grain structure [64,65,71]. The severity of increases with increase in the grain aspect ratio (higher aspect ratio grains results in slower build up of strain), as clearly demonstrated for AA2014-T651 and AA2024-T351 alloys [72]. The results showed that the AA2024-T351, with the higher grain aspect ratio, exfoliated faster than the AA2014-T651 alloy. Another important factor is the heat treatment condition, which can change the microchemistry of the alloy. For example, the effect of T6 and T7 condition on the susceptibility of AA7178 to exfoliation corrosion revealed that the T7 condition was less susceptible than the T6 condition [73]. This was attributed to the observation that over-aging (T7) promoted a more uniform precipitation of anodic phases throughout the matrix when compared to that observed in the T6 condition.

2.4 SUMMARY

It can concluded from the literature review presented above that the localized corrosion behaviour, and the influence of microstructure, of Cu-rich 7XXX alloys, AA7075 in particular, has been extensively studied. In contrast, the localized corrosion behaviour, and the influence of microstructure of Cu-lean AA7XXX alloys has not been given the same consideration. It is clear that the microstructure of AA7XXX alloys is highly influenced by the presence and composition of the second phase particles present in the microstructure. The difference in electrochemical behaviour of second phase particles and matrix play a controlling role in the initiation and propagation of localized corrosion of AA7XXX alloys. It has been found that the Cu content in the generic $Mg(ZnCuAl)_2$ precipitates that form on the grain boundaries plays a controlling role in determining the localized breakdown potential, and, thus the resultant local galvanic corrosion activity that occurs as a consequence. Given the critical role by alloyed Cu content and the lack of information pertaining to the susceptibility to intergranular corrosion and exfoliation corrosion of Cu-lean AA7XXX alloys, there is a need to study the localized corrosion behaviour of AA7003 extrusions in some detail.

3.0 RESEARCH OBJECTIVES

Based on the literature review, it is clear that the susceptibility to intergranular corrosion and exfoliation corrosion of AA7XXX-series alloys, and the corresponding controlling microstructure factors, has been studied in significantly more detail for the Cu-rich alloys than for the Cu-lean alloys. The major difference in the microstructure between Cu-lean and Cu-rich AA7XXX alloys is concluded to be the Cu content of the second phase intermetallic particles found within the matrix and of the second phase strengthening precipitates found within the matrix and on the grain boundaries. This is expected to have important consequences with respect to the susceptibility to intergranular corrosion and exfoliation corrosion of Cu-lean AA7XXX alloys relative to Cu-rich AA7XXX alloys. Considering the significantly ennobled corrosion potentials, and corresponding increased micro-galvanic cell activity, of Cu-containing second phases relative to both the matrix and the solute depleted zones, the Cu-lean alloys are expected to have a lower susceptibility than Cu-rich alloys.

For the use of Cu-lean AA7003 extrusions in automotive bumper assemblies, a key question is then whether the expected lower susceptibility to intergranular corrosion and exfoliation corrosion, relative to Cu-rich AA7XXX alloys, is significant with respect to the in-service corrosion performance. Moreover, considering that the AA7003 extrusion will be exposed to subsequent heat-treatments during the automotive assembly process, another key question is whether or not these subsequent heat treatments affect the susceptibility to these localized forms of corrosion.

The overall objective of this study is to better understand the key structure-performance relationships involved in the intergranular corrosion and exfoliation

corrosion of AA7003 extrusions, as a function of the heat treatment applied. The heat treatments of interest are a naturally-aged T4 (as-extruded) condition, an artificially-aged T6 condition, and an artificially-aged automotive paint-bake condition. The artificially-aged T6 heat treatment corresponds to the proposed post-weld stress relief treatment that the AA7003 bumper beam would be subjected to (by the supplier) if supplied with the crush cans welded in position. In contrast, the artificially-aged automotive paint-bake condition corresponds to the heat treatment that the AA7003 bumper beam would be subjected to if the bumper beam is supplied without the crush cans welded in position.

4.0 EXPERIMENTAL DETAILS

4.1 AA7003 EXTRUDED BUMPER BEAM

All test samples used in this study were prepared from an extruded AA7003 bumper beam provided in the naturally-aged T4 condition by Alcan Automotive Structures & Design (Novi, MI). Figure 3.1 shows a sample of the extruded bumper beam cut in cross-section. The major dimensions are listed on the photograph. Also marked are the two orthogonal directions that defining the cross-section plane shown, namely the LT (longitudinal transverse) and the ST (short transverse) directions. The third orthogonal direction, namely the L (longitudinal) direction is normal to the page. The extrusion direction is parallel to the L direction.

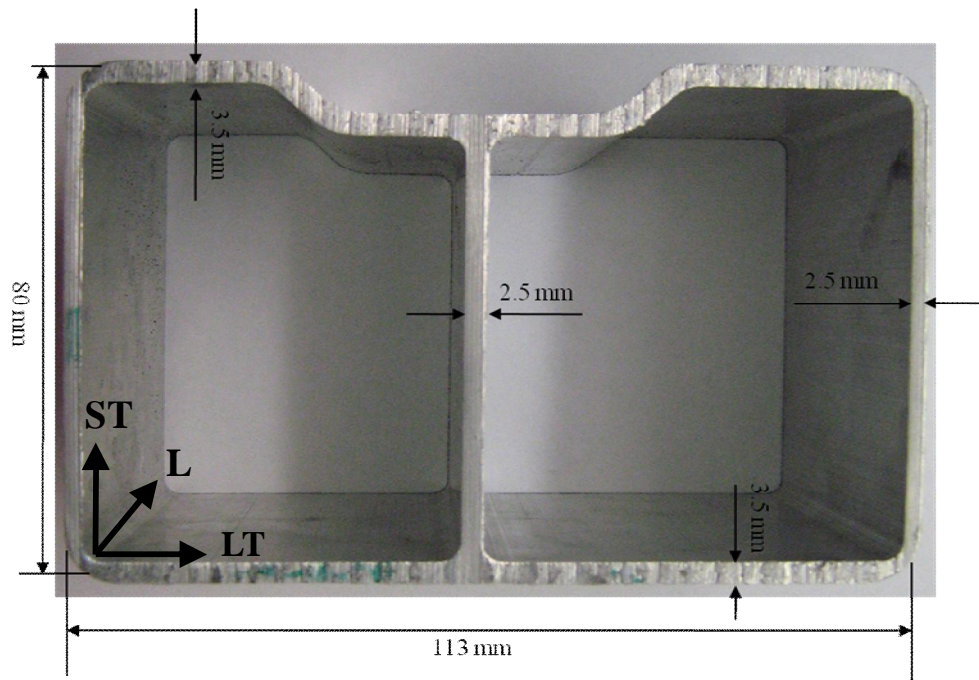


Figure 4.1 Photograph of the extruded bumper beam cut in cross-section, showing the general structure, major dimensions and orientation axis.

The chemical composition of the extruded AA7003 bumper beam was determined using Glow Discharge Optical Emission Spectroscopy (GDOES). A bulk analysis was carried out on two rectangular samples (30 mm x 27 mm x 2.5 mm) cut from the bumper beam. The two test samples were manually grinded to a 4000 grit surface finish using silicon carbide (SiC) paper and water (H_2O) as a lubricant, and then cleaned using a detergent solution. A set of three measurements were taken on each test sample, and the average recorded for the various elements.

All GDOES measurements were made with the power set to 60 W, the pressure set to 900 Pa and relative standard deviation of less than 1. The reference data table for the composition of the Cu-rich AA7075 alloy was used to determine the composition of the AA7003 extrusion samples.

Table 4.1 shows the results of average chemical composition determined using the GDOES technique. Included in the table for comparative purposes is the nominal chemical composition of AA7003, as specified by The Aluminum Association, Inc., [74].

As the table shows, the averaged measured chemical composition of the major alloying elements (Zn, Mg & Cu) is consistent with the nominal composition specified by The Aluminum Association, Inc.

The compositions of all of the remaining elements are below the listed nominal composition limits. The Zr content was not determined because the reference data table for the composition of the Cu-rich AA7075 alloy did not contain Zr.

Table 4.1 Chemical Composition of Extruded AA7003 Bumper Beam by GDOES

Element	Sample 1 (Average)	Sample 2 (Average)	Maximum Nominal Composition [74]
Al	92.5	92.7	Balance
Zn	5.94	5.79	5.0-6.5
Mg	0.98	0.96	0.50-1.0
Cu	0.13	0.13	0.20
Si	0.07	0.06	0.30
Fe	0.16	0.14	0.35
Mn	0.12	0.12	0.30
Zr	Not Determined	Not Determined	0.05-0.25
Ti	0.02	0.02	0.20
Cr	0.08	0.07	0.20

4.2 HEAT TREATMENTS

Test samples were examined and/or tested in one of three heat-treated conditions, namely, a naturally-aged T4 (as-received) condition, an artificially-aged T6 condition, and an artificially-aged paint-bake (PB) condition. The naturally-aged T4 condition is a direct result of the extrusion process itself. Prior to extrusion, the original AA7003 ingot was homogenized at 520°C for 12 h prior to being cut into billets. The billets were extruded at a speed of 7 m/min in a press with the furnace set to 500°C and subsequently cooled on the press using a water spray.

The two artificial aging heat treatments were conducted on AA7003-T4 extrusion samples. The artificially-aged T6 condition involved a subsequent two step heat treatment: the first step at 92°C for 4 h, followed by a second step at 142°C for 12 h. The artificially-aged PB heat treatment involved a single step heat treatment at 185°C for 0.3 h. Both of these artificial aging heat treatments were followed by air-cooling to room temperature. A resistance tube furnace (Paragon) with a built-in microprocessor (Sentry

Xpress 4.0) was used to conduct these artificial aging heat treatments. Samples were wet-ground up to a 4000 grit surface using SiC paper and H₂O as a lubricant, cleaned using a detergent solution and heated in the furnace at a rate of 60°C/h.

4.3 MICROSTRUCTURE EXAMINATION

Small rectangular samples (10 mm x 10 mm x 2.5 mm) were cut from larger rectangular samples (30 mm x 27 mm x 2.5 mm) of the AA7003 extrusion in the naturally-aged T4, artificially-aged T6 and artificially-aged PB heat-treated conditions. These small samples were hot mounted in a phenolic thermosetting resin (BakeliteTM) so as to reveal the L-ST and LT-ST cross-section microstructures of the three heat-treated conditions. Mounted samples were placed into an automatic polisher (RotoPol-31Automatic Polisher) and wet-ground up to 4000 grit surface finish using SiC paper and H₂O as a lubricant, and then sequentially polished using a DAC (3 micron) cloth, a NAP (1 micron) cloth and a colloidal silica (0.05 micron) cloth.

The surface (L-LT) and cross-section (L-ST & LT-ST) microstructures of all mounted samples were examined using an optical light microscope (Leica DM1 5000) equipped with commercial image analysis software package (Clemex Vision Professional Edition). The image analysis software was used to determine the average grain size and the grain size distribution, according to the procedure specified in the ASTM E112 “Standard Test Methods for Determining Average Grain Size” [79]. The image analysis software was also used to determine the grain aspect ratio (length/width) distribution. Mounted cross-sections were chemically etched using Graff reagent, which was prepared by mixing 84 ml of distilled H₂O, 15.5 ml of reagent grade concentrated (70 wt.%) nitric

acid (HNO_3), 0.5 ml of reagent grade concentrated (45 wt.%) hydrofluoric acid (HF), and 3 g of reagent grade chromic oxide (CrO_3), for 45 s.

The appearance and the elemental composition of the second phase (intermetallic) particles present in the cross-section (L-ST & LT-ST) microstructures of the three heat-treated conditions were examined using a scanning electron microscope, (JEOL 7000F SEM), which was instrumented with an energy dispersive X-ray spectrometer (Oxford Instrumnets EDS). Mounted samples were examined in both the as-polished and as-etched condition. Etching involved contacting the mounted samples with an acid solution containing 1 mL reagent grade HF (45 wt.%) dissolved in 100 ml distilled H_2O , for 5 to 10 s. All SEM imaging was conducted with an accelerating voltage of 15 kV, a probe current (Spot Size) of 8 and a working distance of 10 mm.

The grain boundary region, which includes the adjacent SDZ, in the surface (L-LT) layer and the interior (L-LT) microstructures in the three heat-treated conditions was examined using a scanning transmission electron microscope (JEOL 2010F STEM), which was instrumented with an energy dispersive X-ray spectrometer (Oxford Instruments EDS). The procedure used to prepare samples for STEM examination involved the following steps. Samples 10 mm x 15 mm were prepared from larger rectangular samples (30 mm x 27 mm x 2.5 mm) in the naturally-aged T4, artificially-aged T6 and artificially-aged PB heat-treated conditions using a cutting machine (Accutom-5). These samples were then manually grinded to a thickness of about 0.1 mm. Circular discs were then punched out from the thin sheet and subsequently electropolished (Tenupol-5 Electropolisher) in a solution containing 25% reagent grade

HNO₃ (70 wt.%) and 75% reagent grade methanol (CH₃OH) at an applied voltage of 13.5 V and a temperature of -30°C.

Micorhardness (Vickers) measurements (Clemex CMT.HD) were also made on the as-polished mounted cross-section (L-LT & LT-ST) microstructures of the three heat-treated conditions. An average of 20 measurements were made on each sample with a 100 g-load and a 10 s dwell time along lines parallel to the two principle orthogonal directions defining both the L-ST and LT-ST planes.

4.4 ANODIC POLARIZATION MEASUREMENTS

Potentiodynamic anodic polarization curves for the AA7003 extrusion in the three heat-treated conditions were measured in a deaerated 0.5 M NaCl solution with pH 3.56 at room temperature. These measurements were conducted using a standard three electrode test cell with a volumetric capacity of 1000 ml. Working electrodes were prepared by cold mounting a small rectangular sample (1 cm²), cut from the larger rectangular samples (30 mm x 27 mm x 2.5 mm) in the naturally-aged T4, artificially-aged T6 and artificially-aged PB heat-treated conditions, in epoxy. Electrical contact was obtained by soldering a length of copper wire to the back side of the working electrode prior to cold mounting. This copper lead was then inserted into a glass tube, which was sealed to the back of the epoxy mount using more epoxy. All working electrodes prepared in this way were wet-ground to a 4000 grit surface finish using SiC paper and H₂O as a lubricant prior to immersion.

Test solutions were prepared using reagent grade NaCl and distilled H₂O. The pH was adjusted to 3.56 by adding, drop wise, reagent grade HCl. High purity nitrogen gas

was used to deaerate all test solutions for a period of 30 minutes prior to the start of the polarization measurements, and for the duration of the polarization measurement. A fresh solution was used for each measurement.

The procedure involved first recording the corrosion potential for a period of 60 minutes before recording the potentiodynamic polarization behaviour. All polarization curves were measured at a scan rate of 0.2 mV/s using a computer-controlled potentiostat (EG&G PAR 273). Each scan started at a potential -250 mV more negative than the corrosion potential and finished once the current density reached +1 mA/cm². All potentials were measured against an external saturated calomel reference electrode (SCE), which was electrically connected to the test solution using a Luggin salt bridge. The reference potential of a SCE electrode is +241 mV versus the standard hydrogen electrode (SHE). Two graphite rods were used as the counter electrode.

4.5 INTERGRANULAR CORROSION TESTING

The influence of the heat-treated condition on the intergranular corrosion resistance of the AA7003 extrusion was evaluated following the procedure specified in the ASTM G110 “Standard Practice for Evaluating Intergranular Corrosion Resistance of Heat Treatable Aluminum Alloys by Immersion in Sodium Chloride + Hydrogen Peroxide Solution” [80]. Essential details are summarized below.

Triplicate rectangular test samples 37 mm x 20 mm x 2.5 mm in each of the three heat-treated conditions were prepared from the as-received bumper beam. All test samples were cut in a manner that had the long axis parallel to the extrusion direction. Prior to immersion, test samples were first wet-ground up to 4000 grit surface finish

using SiC paper and H₂O as a lubricant, and degreased in reagent grade CH₃OH. Samples were then cleaned in an etching solution for 60 s. The etching solution was prepared by mixing 945 ml of H₂O, 50 ml of reagent grade HNO₃ (70 wt.%) and 5 ml of reagent grade HF (45 wt.%). A heated oil bath was used to maintain the test solution temperature at 93°C. After cleaning, samples were then rinsed in distilled H₂O, immersed in reagent grade HNO₃ (70 wt.%) for 60 s, rinsed again with distilled H₂O and air dried. As a final step, the initial weight of all samples was recorded.

The procedure adopted involved immersing a set of triplicate samples in 1000 mL of the test solution for a period of 24 h. The corresponding surface area to volume ratio was about 18.9 mL/cm², which is well above the minimum ratio of 5 mL/cm² specified in the standard procedure. Test solutions were prepared by dissolving and diluting 57 g of reagent grade NaCl and 10 ml of reagent grade H₂O₂ in distilled H₂O to 1000 mL. No attempt was made to aerate, deaerate or stir the test solutions. A heating mantle was used to maintain the test solution at 30°C.

Upon removal from the test solution, all samples were rinsed with distilled H₂O, dried with absorbent wipes, and reweighed before being bisected along the short axis (perpendicular to the extrusion direction) and cold mounted and polished in cross-section following the procedure described previously. The mounted cross-sections were then observed using light optical microscopy (Nikon eclipse LV 100 & Leica DM1 5000) to document and quantify the maximum depth of attack.

4.6 EXFOLIATION CORROSION TESTING

The influence of the heat-treated condition on the exfoliation corrosion resistance of the AA7003 extrusion was evaluated following the procedure specified in the ASTM G34 “Standard Test Method for Exfoliation Corrosion Susceptibility in 2XXX and 7XXX Series Aluminum Alloys (EXCO Test)” [81]. Essential details are summarized below.

Triplicate rectangular test samples 60 mm x 30 mm x 2.5 mm in each of the three heat-treated conditions were prepared from the as-received bumper beam. All test samples were cut in a manner that had the long axis perpendicular to the extrusion direction. Prior to immersion, test samples were wet-ground up to 4000 grit surface finish using SiC paper and H₂O as a lubricant, degreased in reagent grade CH₃OH, dried with absorbent wipes, and weighed.

The procedure adopted involved immersing a set of triplicate samples in 2000 mL of the test solution at room temperature for a period of 48 h. The corresponding surface area to volume ratio was about 16.5 mL/cm², which is within the volume-to-metal surface area ratio range of 10 to 30 mL/cm² specified in the standard procedure. Test solutions were prepared by dissolving and diluting 468 g of reagent grade NaCl, 100 g reagent grade potassium nitrate (KNO₃) and 12.6 mL of reagent grade HNO₃ (70 weight %) in distilled H₂O to 2000 mL. No attempt was made to aerate, deaerate or stir the test solutions.

Upon removal from the test solution, all samples were immediately photographed. Samples were then rinsed with distilled H₂O, dried with absorbent wipes, and reweighed before being bisected along the short axis (parallel to the extrusion direction)

and cold mounted and polished in cross-section following the procedure described previously. The mounted cross-sections were then observed using light optical microscopy (Nikon eclipse LV 100 & Leica DM1 5000) to document and quantify the maximum depth of attack.

5.0 RESULTS

5.1 METALLOGRAPHIC EXAMINATION

Figure 5.1 shows the orthogonal metallographic microstructures of the AA7003 extrusion samples in the three heat-treated conditions under study. All microstructures exhibit similar features. The surface (L-LT) microstructures readily show an elongated grain structure in the direction parallel to the extrusion direction. The cross-section (LT-ST & L-ST) microstructures readily show a dual grain structure, consisting of a fibrous non-recrystallized grain structure in the interior, and a coarse recrystallized surface layer ranging in thickness from about 50 to 70 microns (Figure 1d). The cross-section microstructures also reveal the presence of randomly-distributed, microsized second phase particles. It is noted here that the grain structure of aluminum alloy extrusions may become recrystallized, partly recrystallized or fibrous (non-recrystallized) depending on the chemical composition of the alloy, the preheat treatments before the extrusion process and the extrusion parameters (speed, temperature and die design) [75]. Therefore, the dual grain microstructure observed in cross-section is not unexpected.

Figure 5.2 shows the measured grain size distributions of the cross-section microstructures observed in the three heat-treated conditions. Note that the distributions plotted correspond to the fibrous, non-recrystallized grain structure in the interior of the cross-section. Each grain size bin contains a range of 1 μm . A similar bimodal grain size distribution is observed, regardless of the heat-treated condition and of the cross-section microstructure. The majority of grain sizes occur in one cluster ranging from 10 to 18 μm , whereas a small cluster of grain sizes exists ranging from 21 to 25 μm with relative

error being less than 10%.. The average grain size measured in the L-ST microstructure is 15.3 μm , 14.8 μm , and 15.1 μm for the T4, T6 and PB heat-treated condition, respectively. In the LT-ST microstructure, the average grain size is 14.3 μm , 15.3 μm , and 15.3 μm for the T4, T6 and PB heat-treated condition, respectively.

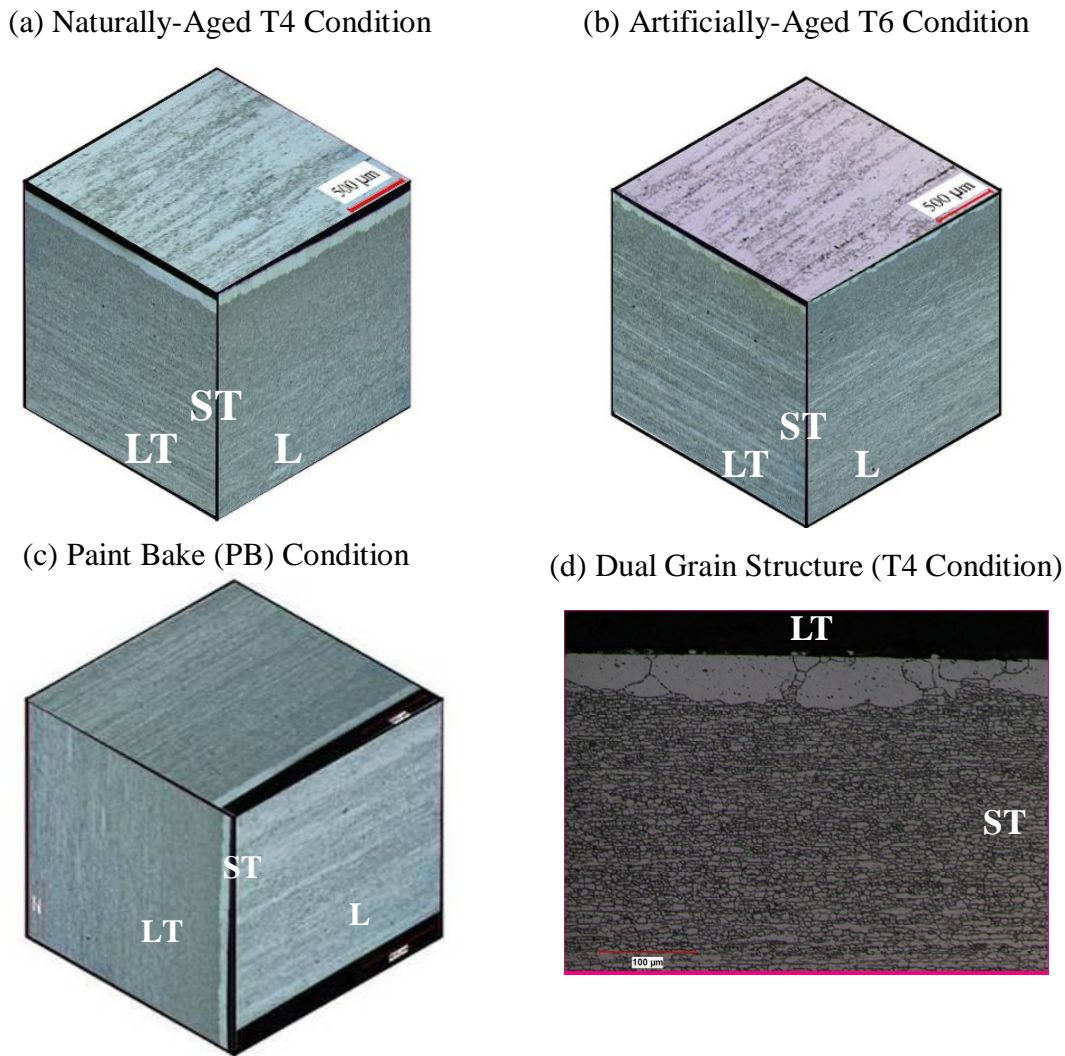


Figure 5.1 Microstructure of the three orthogonal sections of the AA7003 extrusion in the (a) naturally-aged T4 heat-treated (as-received) condition, (b) artificially-aged T6 heat-treated condition, and (c) artificially-aged paint bake heat-treated condition. Magnified view of the ST-LT microstructure in the T4 heat-treated condition (d).

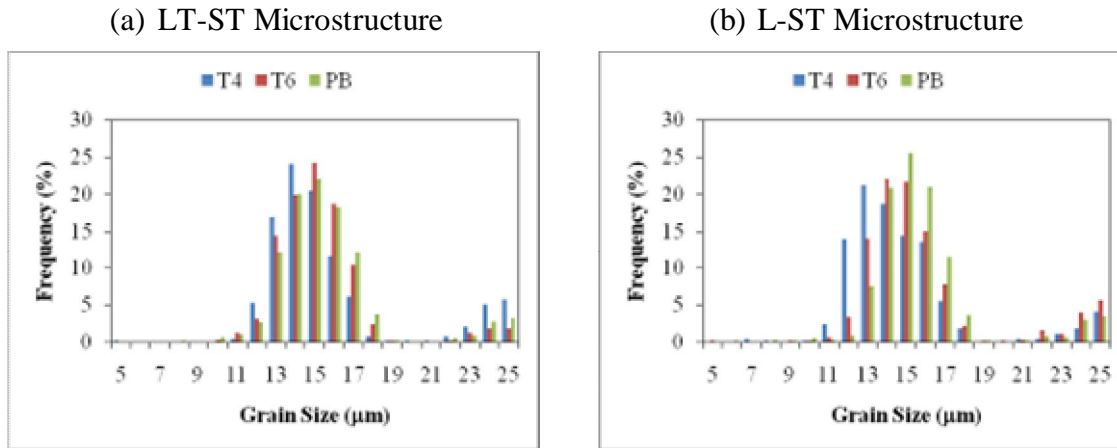


Figure 5.2 Bar charts showing influence of the heat-treated condition on the AA7003 extrusion grain size distribution of the (a) LT-ST cross-section microstructure, and (b) L-ST cross-section microstructure.

The aspect ratio distributions of the grains in the cross-section microstructures observed in the three heat-treated condition are shown in Figure 5.3. Again, all distributions plotted correspond to the fibrous, non-recrystallized grain structure present in the interior of the cross-section. Each grain aspect ratio bin contains a range of 0.1. A similar unimodal, albeit wide, distribution is observed for the aspect ratio of the grains, regardless of the heat-treated condition and cross-section microstructure. The average grain aspect ratios in the L-ST microstructure are 1.6, 1.7 and 1.6 for the T4, T6 and PB heat-treated condition, respectively and relative error less than 10%. In the LT-ST microstructure, the average grain size ratio is 1.6 for all three heat-treated conditions. An aspect ratio of less than unity is not observed in any of the microstructure areas examined.

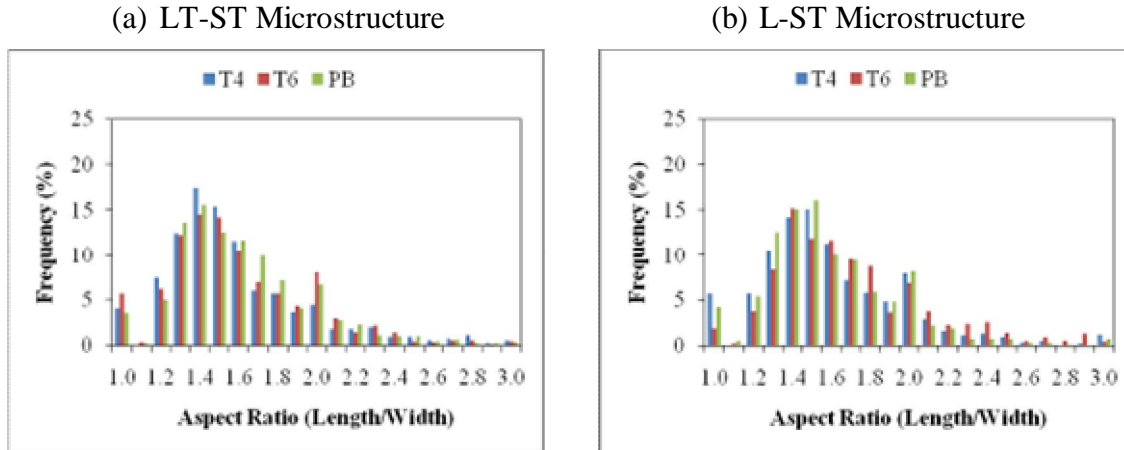


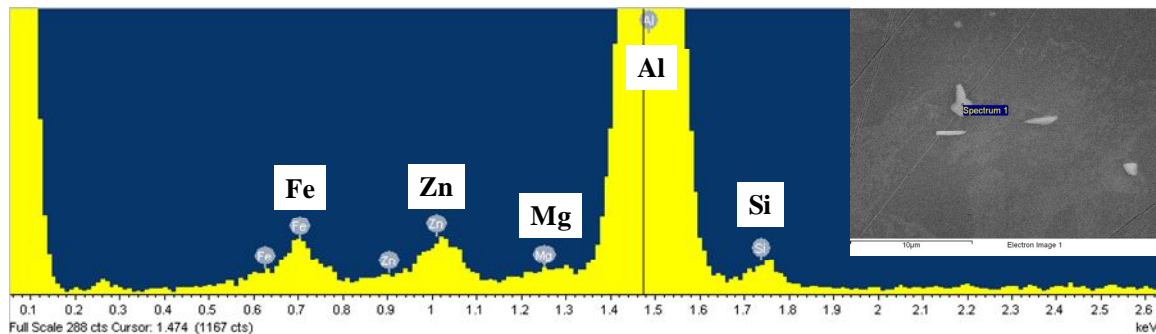
Figure 5.3 Bar charts showing influence of the heat-treated condition on the AA7003 extrusion grain aspect ratio of the (a) LT-ST cross-section microstructure, and (b) L-ST cross-section microstructure.

5.2 SEM/EDS EXAMINATION OF SECOND PHASE PARTICLES

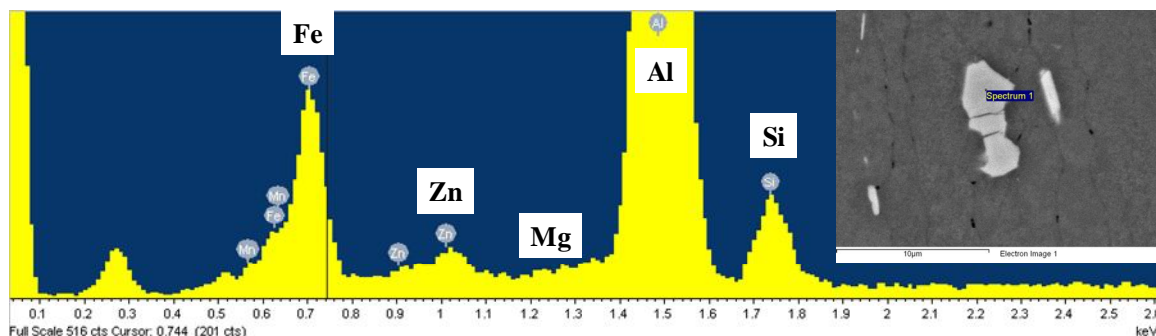
Figure 5.4 & 5.5 shows the typical appearance and the corresponding elemental (EDS) analysis of the irregular-shaped and rectangular-shaped second phase particles, respectively, observed in the surface (L-LT) microstructure for the three heat-treated conditions. Two types of second phase particles are observed, namely a larger, darker, irregular-shaped phase and a smaller, brighter, rectangular-shaped phase. In addition to the major alloy elements (Al, Zn & Mg), the larger, darker, irregular-shaped phase is enriched with both Fe and Si, whereas the smaller, brighter, rectangular-shaped phase is enriched with just Fe. A detailed quantification of these peak intensities was not attempted. However, based on the existing knowledge regarding the composition of second phase particles in AA7XXX alloys [16,21-23,25,26], it is reasonable to assume that the larger irregular-shaped phase is a $\text{Al}_{12}(\text{Fe,Mn})_3\text{Si}$ intermetallic phase, whereas the smaller rectangular-shaped phase is a Al_3Fe intermetallic phase. Note that a distinct Cu

peak was not observed in any of the EDS analysis conducted on these second phase particles.

(a) Naturally-Aged T4 Condition



(b) Artificially-Aged T6 Condition



(c) Artificially-Aged PB Condition

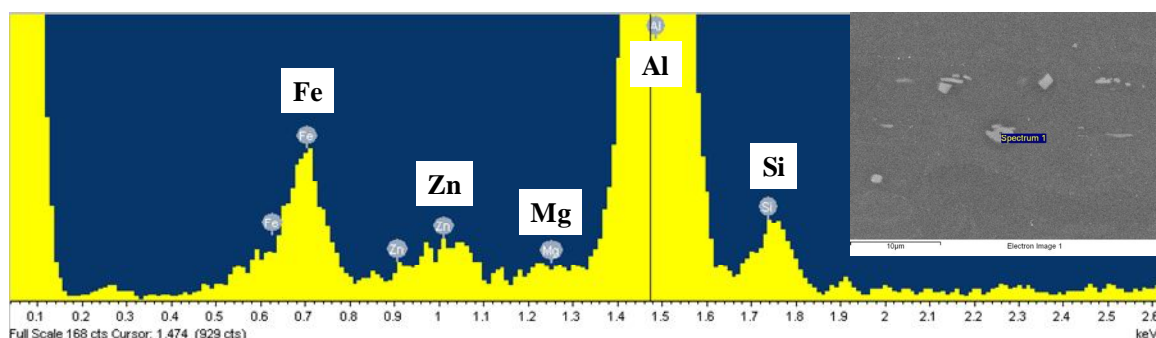
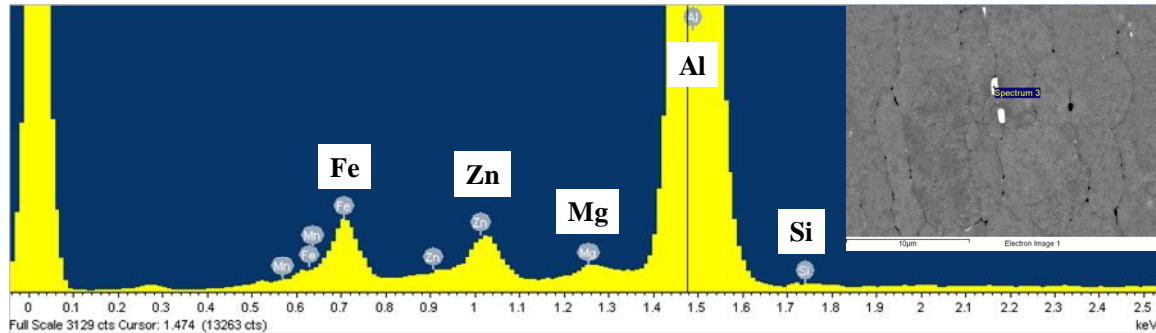
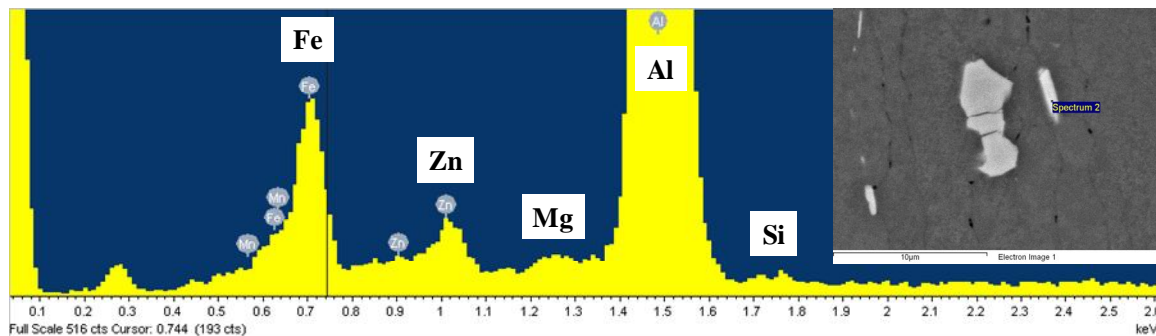


Figure 5.4 Typical appearance and elemental composition of the randomly-distributed, micro-sized irregular-shape second phase particles found on the surface (L-LT plane) microstructure of the AA7003 extrusion in the (a) naturally-aged T4 heat-treated (as-received) condition, (b) artificially-aged T6 heat-treated condition, and (c) artificially-aged paint bake (PB) condition.

(a) Naturally-Aged T4 Condition



(b) Artificially-Aged T6 Condition



(c) Artificially-Aged PB Condition

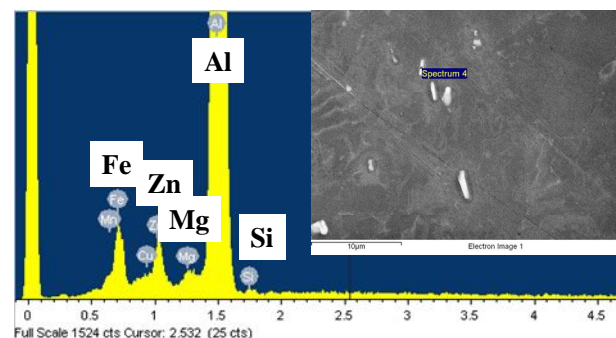


Figure 5.5 Typical appearance and elemental composition of the randomly-distributed, micro-sized rectangular-shape second phase particles found on the surface (L-LT plane) microstructure of the AA7003 extrusion in the (a) naturally-aged T4 heat-treated (as-received) condition, (b) artificially-aged T6 heat-treated condition, and (c) artificially-aged PB condition.

5.3 STEM/EDS EXAMINATION OF GRAIN BOUNDARIES

Figure 5.6 shows the bright-field micrographs of the grain boundary regions in the coarse, recrystallized surface layer, and in the fibrous, non-recrystallized interior for the three heat-treated conditions. All micrographs show similar features, namely the presence of fine hardening precipitates in the matrix, a SDZ adjacent to the grain boundaries, and precipitates on the grain boundaries. From inspection, the apparent size of the fine hardening matrix precipitates is largest in the T6 heat-treated condition and smallest in the T4 heat-treated condition. The apparent width of SDZ is largest for the T6 heat treated condition (about 40 nm) and smallest for the T4 heat-treated condition (about 2 nm). The majority of grain boundary precipitates observed in both the surface layer and in the interior are elliptically-shaped. The spacing between these precipitates is largest in the T6 heat-treated condition and smallest for the T4 heat-treated condition.

Table 5.1 summarizes the elements present in the alloy that are significantly enriched (relative to the matrix) across the grain boundary regions in the six STEM samples examined, as identified by an EDS line scan analysis. The complete set of STEM micrographs showing the location of the line scan and the corresponding EDS results for the various elements detected is provided in Appendix 1. All line scans across the elliptically-shaped grain boundary precipitates show a significant enrichment of the major alloying elements Zn and Mg relative to the matrix. The exception is the line scan across the grain boundary precipitate in the surface layer of the T4 heat-treated condition, in which Zr and Si, rather than Zn and Mg, are enriched relative to the matrix. The more striking observation is the enrichment of Cu across the grain boundary regions of the three heat-treated conditions. In the naturally-aged T4 condition, Cu is enriched within

the SDZ of both the surface layer and interior. In the artificially-aged PB condition, Cu is enriched in SDZ in the surface layer, whereas it is enriched in the grain boundary precipitate in the interior. In contrast there is no indication of Cu enrichment (or depletion) in either the SDZ or in the grain boundary precipitate examined in the artificially-aged T6 heat-treated condition.

Table 5.1 Summary of Enriched Elements (Relative to Matrix) in Grain Boundary Region

Heat-Treated Condition	Surface Layer		Interior	
	SDZ	GB Precipitate	SDZ	GB Precipitate
T4	Cu	Si, Zr	Cu	Zn, Mg
T6	None	Zn, Mg	None	Zn, Mg
PB	None	Zn, Mg, Cu	Cu	Zn, Mg

5.4 MICROHARDNESS MEASUREMENTS

Table 5.2 lists the average and standard deviation values for the sets of Vickers microhardness measurements made on the cross-section microstructures of the three heat-treated conditions. The data show that, for both the LT-ST and L-ST microstructures, the T6 heat-treated condition has the highest microhardness, whereas the T4 heat-treated condition has the lowest microhardness. The data also show that, for a given heat-treated condition, the two cross section microstructures exhibit a similar microhardness.

Table 5.2 Microhardness (H_v) Data for Cross-Section Microstructures

Heat-Treated Condition	LT-ST Microstructure H_v			L-ST Microstructure H_v		
	Measurement Number	Average	Standard Deviation	Measurement Number	Average	Standard Deviation
T4	24	112	5	23	110	3
T6	22	145	5	22	148	6
PB	24	130	10	23	127	7

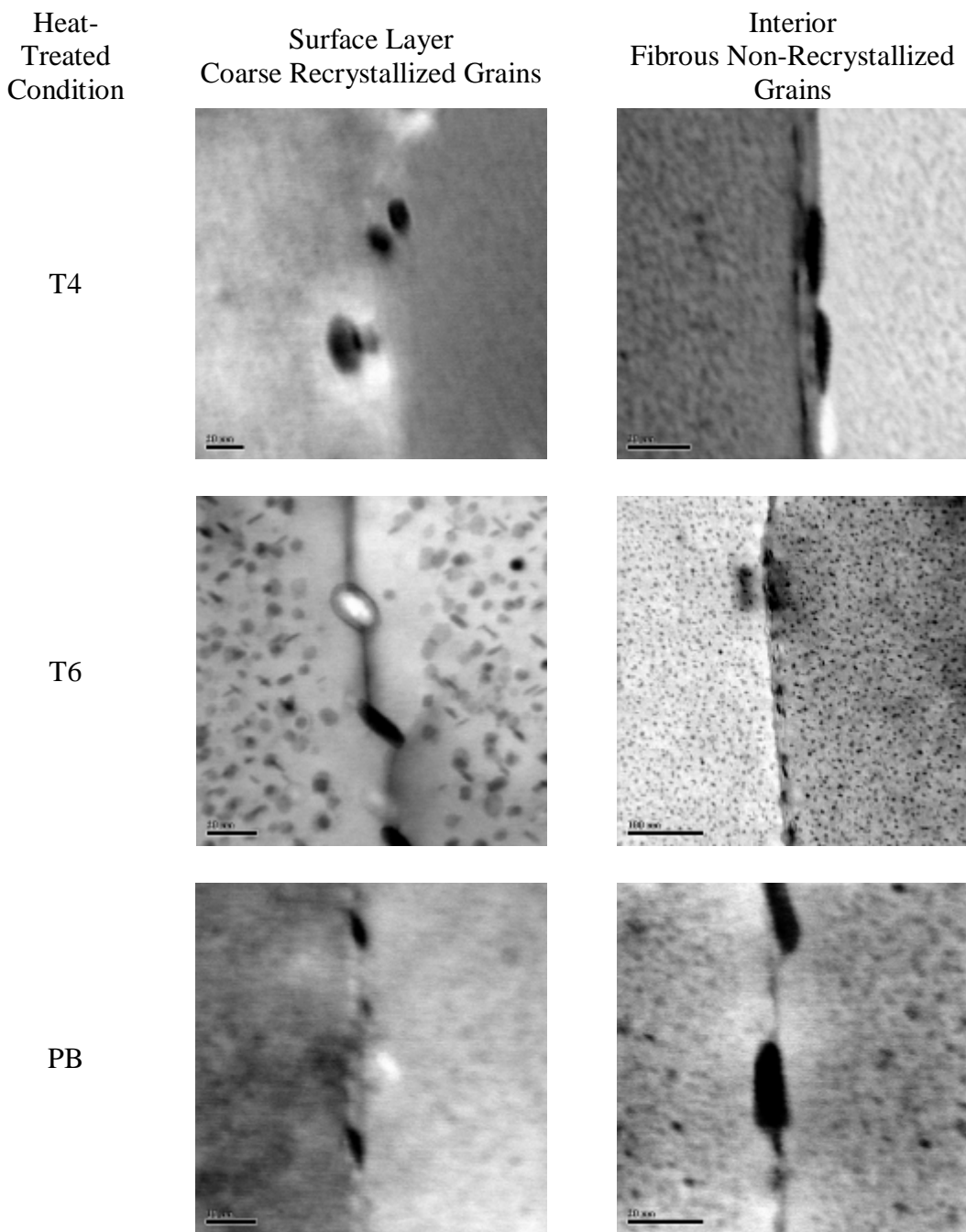


Figure 5.6 STEM micrographs of the grain boundary regions in the coarse, recrystallized surface layer and the fibrous, non-recrystallized interior for the naturally-aged T4, artificially-aged T6 and artificially-aged paint bake (PB) heat-treated conditions.

5.5 ANODIC POLARIZATION MEASUREMENTS

Figure 5.7 shows the anodic polarization curves for the AA7003 extrusion with the three heat-treated conditions in deaerated 0.5 M NaCl solution with a pH 3.56. One set of three curves was recorded with the coarse, recrystallized (L-LT) surface layer exposed to the solution, and a second set with the fibrous, non-recrystallized (L-LT) interior exposed to the solution. All six curves show a similar anodic polarization response, namely a passive region at potentials more positive than the corrosion potential (E_{corr}), in which the current density is weakly dependent on the applied potential, and a single breakdown potential (E_b), above which a sharp increase in current density occurs with a further increase in the applied potential.

The data for the corrosion potentials and breakdown potentials are listed in Table 5.3. Based on the differences in potential, relative to the naturally-aged T4 microstructure (Δ_{T4}), the corrosion potential (-37 mV to -76 mV) is significantly more sensitive to the heat-treated condition than the breakdown potential (-5 mV to +5 mV) for both the surface layer and interior microstructures. Both of the artificially-aged surface layer and interior microstructures exhibit a more negative corrosion potential than the naturally-aged T4 microstructure. In general the surface layer microstructure of a given heat-treated condition exhibits a more negative corrosion potential and a more positive breakdown potential than the interior microstructure.

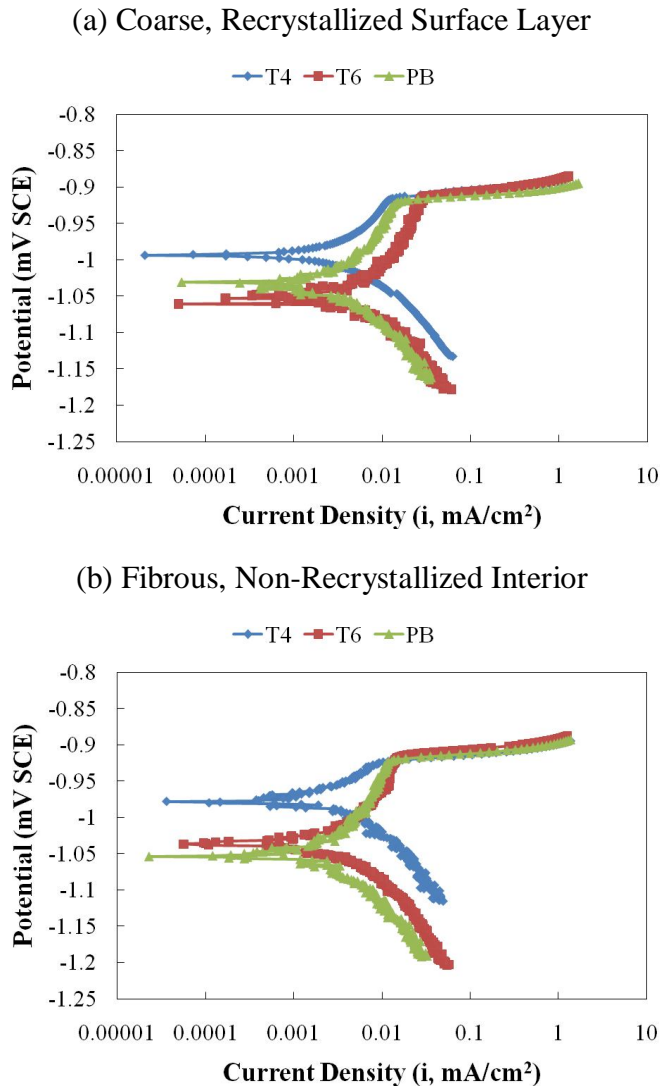


Figure 5.7 Potentiodynamic polarization curves for AA7003 extrusion with the three heat-treated conditions in deaerated 0.5 M NaCl solution with a pH 3.56 with (a) coarse, recrystallized (L-LT) surface layer exposed to the solution, and (b) fibrous, non-recrystallized (L-LT) interior exposed to the solution.

Table 5.3 Effect of Heat-Treated Condition on Corrosion and Breakdown Potentials for AA7003 Extrusion in Deaerated 0.5 M NaCl at pH 3.56

Heat-Treated Condition	(L-LT) Surface Layer				(L-LT) Interior			
	E_{corr} mVSCE	Δ_{T4} mV	E_b mVSCE	Δ_{T4} mV	E_{corr} mVSCE	Δ_{T4} mV	E_b mVSCE	Δ_{T4} mV
T4	-994	---	-910	---	-978	---	-925	---
T6	-1061	-67	-905	+5	-1037	-59	-920	+5
PB	-1031	-37	-912	-2	-1054	-76	-930	-5

A visual assessment of the electrode surfaces was conducted after potentiodynamically polarizing to a current density of 1 mA/cm^2 to assist in determining the corrosion form responsible for the breakdown potential observed. Figure 5.8 shows the surface appearance of all six AA7003 extrusion electrodes that were polarized in this manner. Many pits were observed on the surface of each electrode after this treatment.

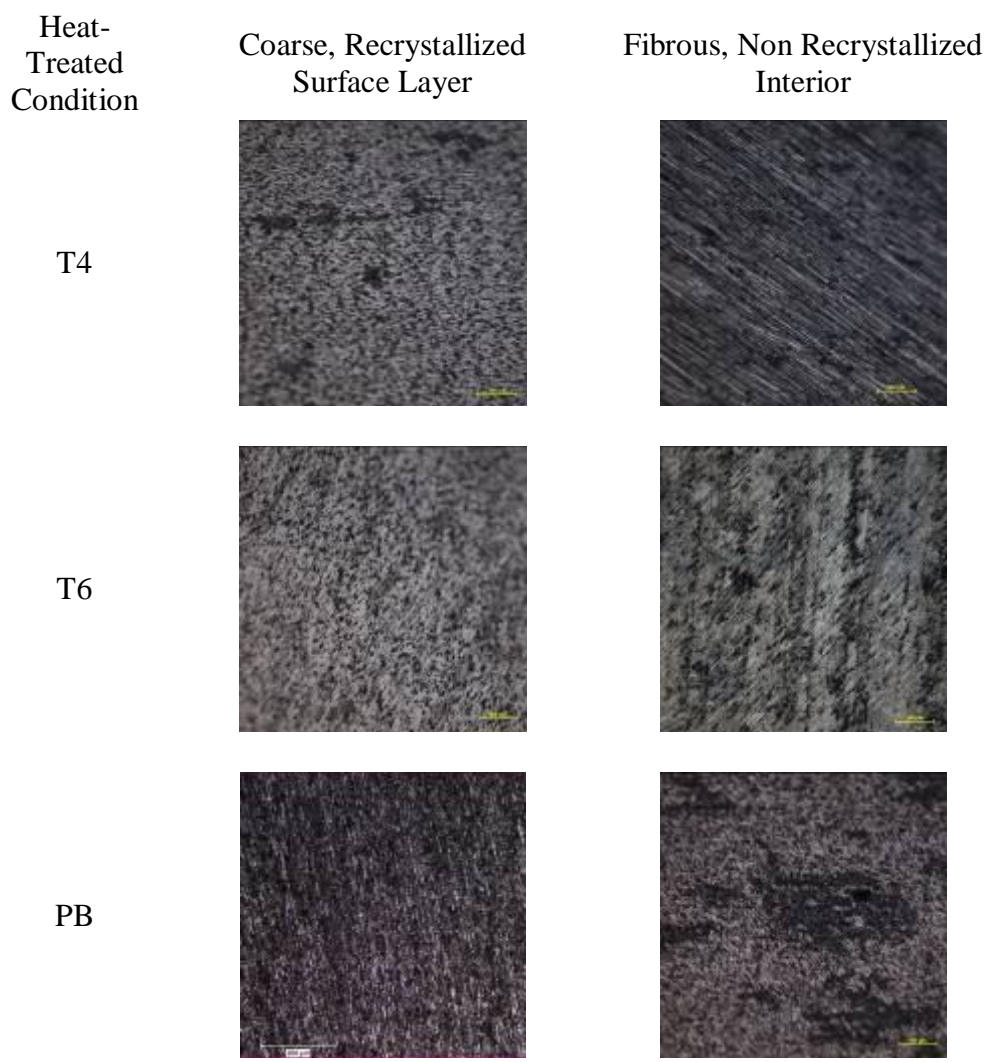


Figure 5.8 Photographs of the exposed surface of the AA7003 extrusion electrodes in the three heat-treated conditions after exposure potentiodynamic anodic polarization to a current density of 1 mA/cm^2 in deaerated 0.5 M NaCl solution with a pH 3.56 at room temperature.

5.6 ASTM G110 – INTERGRANULAR COROSION TEST

Figure 5.9 shows a bar chart comparing the average maximum depth of attack data for the AA7003 extrusion with the three heat-treated conditions, after exposure to the ASTM G110 test solution (57 g NaCl and 10 ml of H₂O₂ diluted with H₂O to 1000 mL) for 24 h at 30°C. Superimposed onto both charts as uncertainty bars are the values for the highest and lowest values for the triplicate set of samples tested in each heat-treated condition.

Measurements in both directions indicate that the maximum depth of intergranular corrosion attack is larger in the naturally-aged T4 condition than it is in either of the two artificially-aged conditions. Of the two artificially-aged heat treatments, the PB condition appears to have the larger maximum depth of intergranular corrosion attack. At least this is the case for measurements in the ST direction, in which there is no overlap in the range (uncertainty). No clear observation can be extracted about the influence of direction of the propagation of intergranular corrosion, since it is found to have an accelerating influence in the naturally aged T4 condition and the artificially-aged PB condition, whereas it has essentially no influence in the artificially-aged T6 condition.

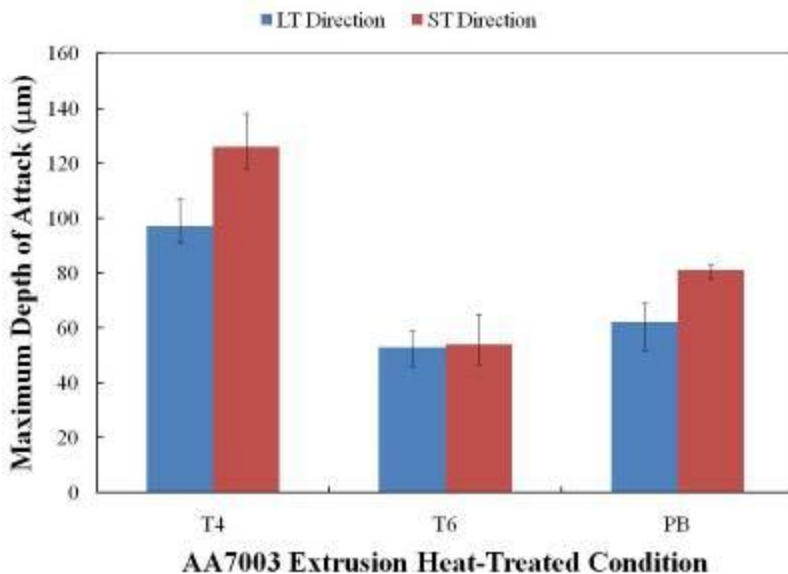


Figure 5.9 Bar chart comparing the influence of heat-treated condition and propagation direction on the maximum depth of attack observed in AA7003 extrusion after exposure to the ASTM G110 test solution (57 g NaCl and 10 ml of H₂O₂ diluted with H₂O to 1000 mL) for 24 h at 30°C.

The cross-section of the corrosion observed in the LT and ST direction in the coupon with the largest measured maximum depth of attack is shown in Figure 5.10 for each of the three heat-treated conditions. The morphology of attack is distinctly different for each of the two propagation directions. In the LT direction (originating from the side of the exposed coupon), the morphology of attack is predominantly intergranular. In contrast, the morphology observed in the ST direction (originating from the face of the exposed coupon) is predominantly pit-like and it is restricted to the coarse recrystallized surface layer. However, there is some evidence of intergranular corrosion at the corrosion front (at the base of the pits).

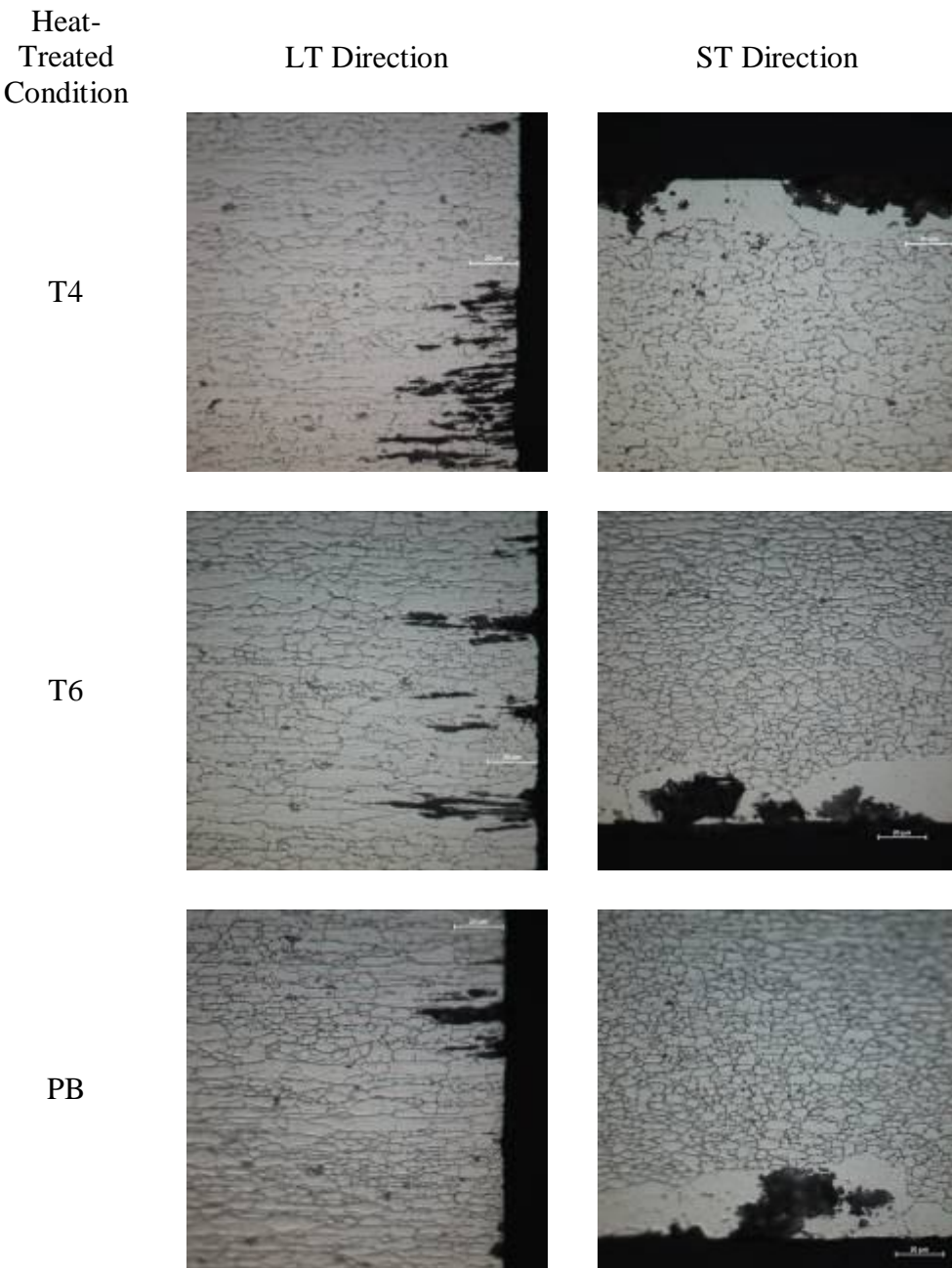


Figure 5.10 Cross-section (LT-ST) micrographs of the AA7003 extrusion coupon in the three heat-treated conditions, with the maximum depth of attack after exposure to the ASTM G110 test solution (57 g NaCl and 10 ml of H₂O₂ diluted with H₂O to 1000 mL) for 24 h at 30°C.

5.7 ASTM G34 – EXFOLIATION CORROSION TEST

Photographs of the triplicate sets of the AA7003 extrusion coupons in the three heat-treated conditions are shown in Figure 5.11, immediately after exposure to ASTM G34 test solution (468 g NaCl, 100 g KNO₃ and 12.6 mL 70 wt.%-HNO₃ diluted in distilled H₂O to 2000 mL) at room temperature for 48 h. Based on a visual assessment, all nine coupons are assigned the same severity of exfoliation corrosion rating of EB (Moderate)/P (Pitting).

Figure 5.12 shows a bar chart comparing the average maximum depth of attack data for the AA7003 extrusion with the three heat-treated conditions, after exposure to the ASTM G34 test solution at room temperature for 48 h. Superimposed onto both charts as uncertainty bars are the values for the highest and lowest values for the triplicate set of samples tested in each heat-treated condition. The bar shows that the heat-treated condition has a significant influence on the maximum depth of attack. Note that the data is only recorded for propagation in the L direction, since this is the predominant propagation direction regardless of whether corrosion originated from the face or the side of the coupon.

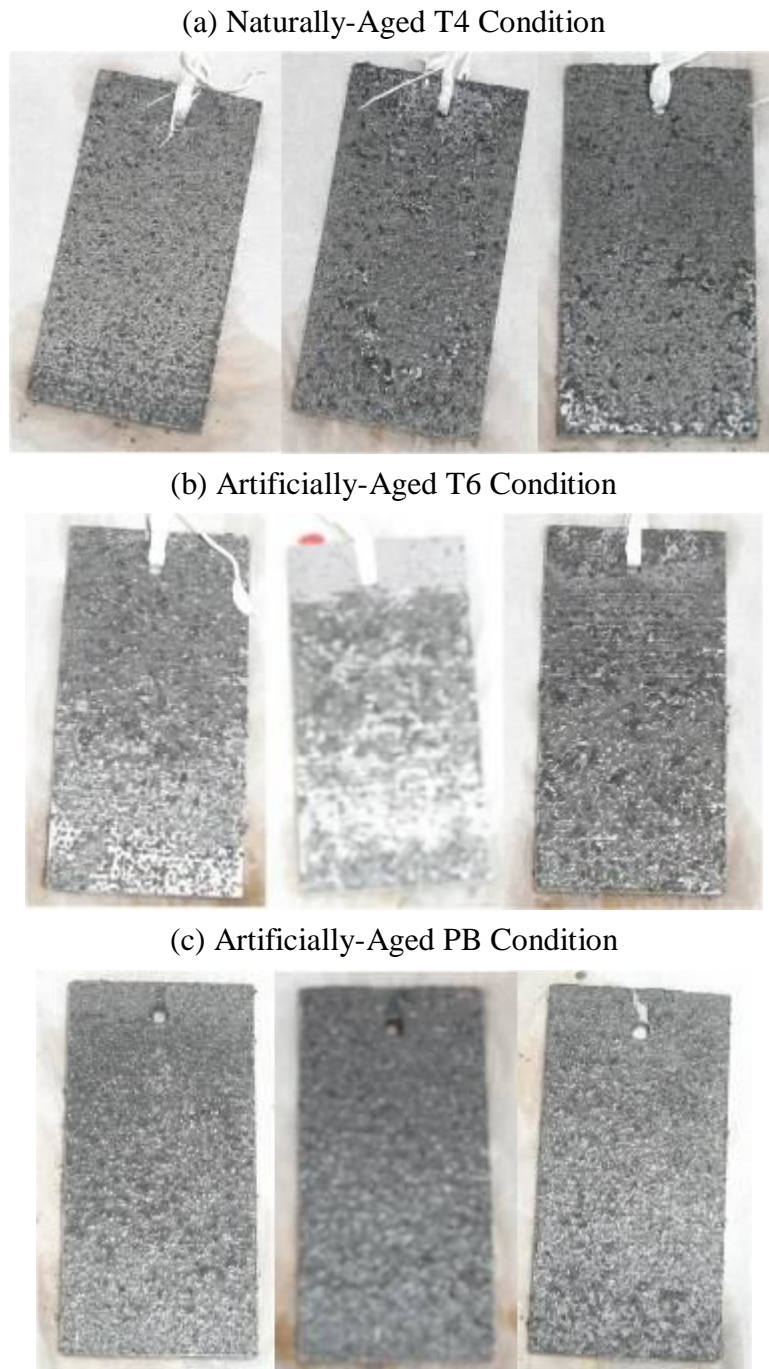


Figure 5.11 Photographs of the triplicate sets of the AA7003 extrusion coupons in the (a) naturally-aged T4 condition, (b) artificially-aged T6 condition, and (c) artificially-aged PB condition, immediately after exposure to ASTM G34 test solution (468 g NaCl, 100 g KNO₃ and 12.6 mL 70 wt.%-HNO₃ diluted in distilled H₂O to 2000 mL) at room temperature for 48 h.

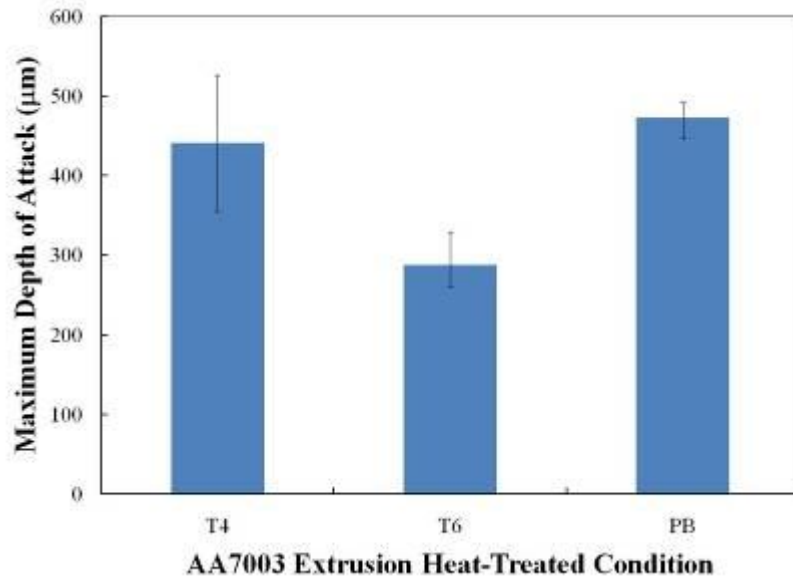


Figure 5.12 Bar chart comparing the influence of heat-treated condition on the maximum depth of attack observed in AA7003 extrusion after exposure to the ASTM G34 test solution (468 g NaCl, 100 g KNO₃ and 12.6 mL 70 wt.%-HNO₃ diluted in distilled H₂O to 2000 mL) at room temperature for 48 h.

The cross-section of the exfoliation corrosion observed in the coupon with the largest measured maximum depth of attack is shown in Figure 5.13 for each of the three heat-treated conditions. The morphology of attack is similar in each of the three heat-treated conditions. It is predominantly pit-like, but with the corrosion front (at the base of the pits) propagating along grain boundaries that are parallel to the extrusion directions. The lower magnification micrographs clearly show that the depth of attack is largest for the artificially-aged PB condition, whereas it is lowest for the naturally-aged T4 condition. The higher magnification micrographs for each of the three heat-treated conditions clearly show the “peeling” feature characteristic of exfoliation corrosion. .

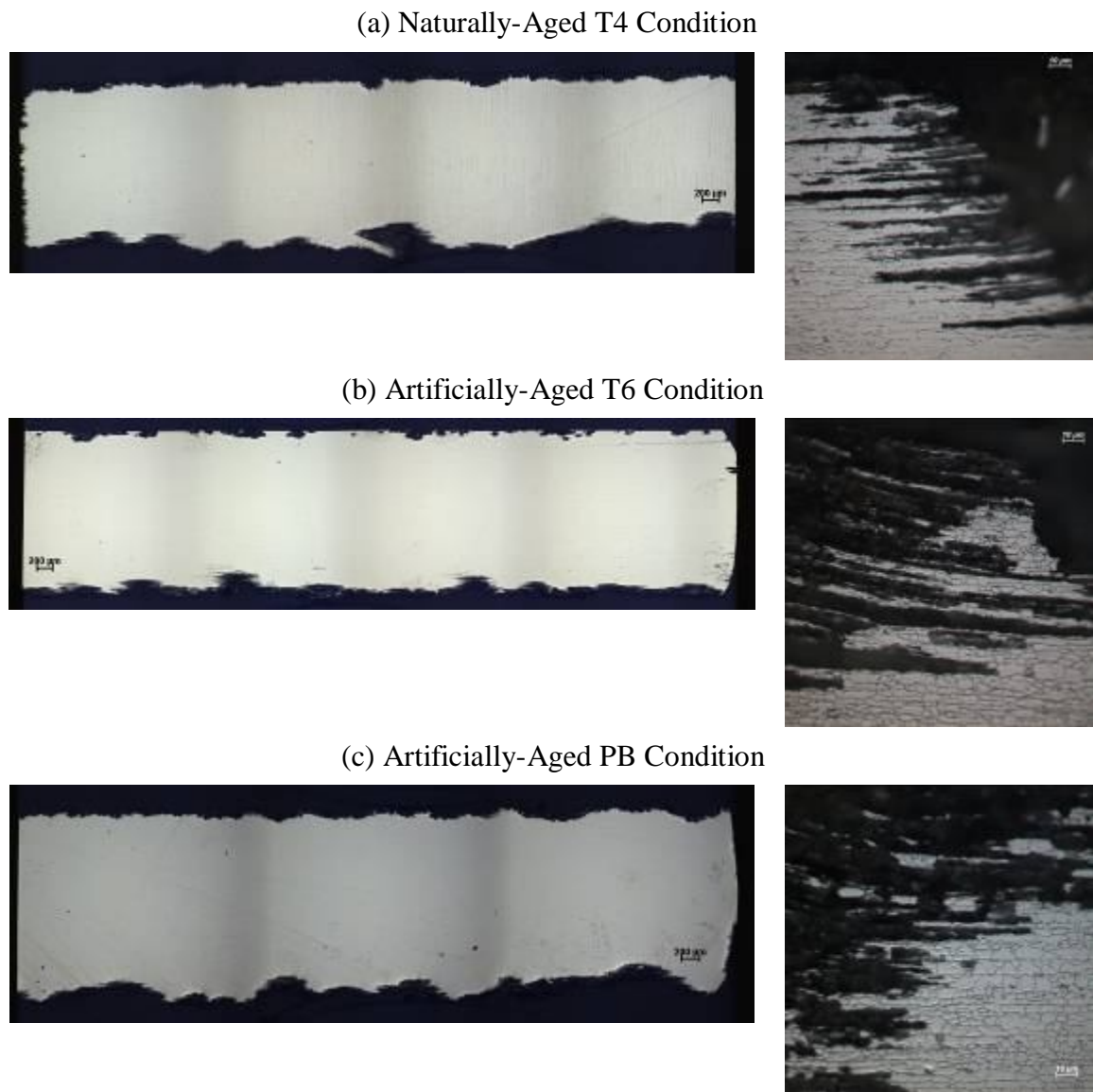


Figure 5.13 Cross-section (L-ST) micrographs of the AA7003 extrusion coupon in the (a) naturally-aged T4 condition, (b) artificially-aged T6 condition, and (c) artificially-aged PB condition, with the maximum depth of attack after exposure to ASTM G34 test solution (468 g NaCl, 100 g KNO₃ and 12.6 mL 70 wt.%-HNO₃ diluted in distilled H₂O to 2000 mL) at room temperature for 48 h.

6.0 DISCUSSION

A major objective of this study is to better understand the key structure-performance relationships involved in the intergranular corrosion and exfoliation corrosion of AA7003 extrusions, as a function of the heat treatment applied. The heat treatments of interest are a naturally-aged T4 (as-extruded) condition, an artificially-aged T6 condition, and an artificially-aged automotive paint-bake condition. The artificially-aged T6 heat treatment corresponds to the proposed post-weld stress relief treatment that the AA7003 bumper beam would be subjective to (by the supplier) if supplied with the crush cans welded in position. In contrast, the artificially-aged automotive paint-bake condition corresponds to the heat treatment that the AA7003 bumper beam would be subjective to if the bumper beam is supplied without the crush cans welded in position. In this context, the influence of heat-treated condition on the microstructure of the AA7003 extrusion and the corresponding corrosion behaviour is discussed separately below.

6.1 EFFECT OF HEAT TREATMENT ON MICROSTRUCTURE

It is generally accepted that for heat treatable AA7XXX alloys that the age hardening at temperatures between 100°C and 200°C results from the formation of the intermediate non-equilibrium η' -MgZn₂ phase, which may later transform to the equilibrium η -MgZn₂ phase [9]. The crystal structure of the non-equilibrium η' -MgZn₂ phase is hexagonal, which is similar to the equilibrium phase η -MgZn₂ phase, but with a slight difference in crystal lattice parameters. It is this difference in crystal lattice that is believed to be responsible for the increase in strength despite having the same composition as the equilibrium η -MgZn₂ [24-29,30-32,39]. Since this phase has

considerable solubility for Cu and Al, the generic composition has been considered to be $Mg(Zn,Cu,Al)_2$ [14].

Considering that the post-weld stress-relief heat treatment and the paint-bake cycle heat treatment are both artificially-aging treatments, they should both increase the strength of the AA7003 extrusion through the formation of the intermediate non-equilibrium η' -MgZn₂ phase. The microhardness measurements made on the cross-section microstructures for the three AA7003 heat-treated conditions (Table 5.2) certainly show this to be the case. Both of the artificially-aged conditions (T6 & PB) exhibited a higher microhardness than the naturally-aged T4 condition. Of the two artificially-aged conditions, the T6 peak aging condition exhibited the higher microhardness. Moreover, the measurements indicate that the microhardness is isotropic with respect to the two cross-section microstructures (planes), for each of the three heat-treated conditions.

It follows naturally that the relative differences in microhardness observed is related to the differences in the microstructure, and the size and distribution of the fine generic $Mg(Zn,CuAl)_2$ precipitates in particular. In this context, the results of the grain boundary examinations using the STEM coupled with EDS is of paramount importance in rationalizing the influence of heat treatment on the microstructure. However, a discussion of the influence of heat treatment on the grain size and grain aspect ratio distribution and second phase intermetallic particles is just as important when rationalizing the influence of heat treatment on the corrosion behaviour.

Based on the results of the optical light microscopy and corresponding image analysis conducted to characterize the three heat-treated microstructures of the AA7003 extrusion, it is clear that the two artificially-aged heat treatments had essentially no

influence on the dual grain structure (Figure 5.1), interior grain size and distribution (Figure 5.2), and the interior grain aspect ratio and distribution (Figure 5.3) observed in the microstructure of the naturally-aged T4 condition. The dual grain structure observed in cross-section, regardless of the heat-treated condition, consists of a fibrous non-recrystallized grain structure in the interior, and a coarse recrystallized surface layer ranging in thickness from about 50 to 70 microns (Figure 5.1d). Again, it is noted that the grain structure of aluminum alloy extrusions may become recrystallized, partly recrystallized or fibrous (non-recrystallized) depending on the chemical composition of the alloy, the preheat treatments before the extrusion process and the extrusion parameters (speed, temperature and die design) [66].

High strength AA7XXX alloys are often used in the rolled or extruded conditions, in which the corresponding microstructure is elongated and anisotropic. Typically, grains tend to be elongated significantly more so in the L and LT directions, leading to a relatively large aspect ratio, and tend to be more elongated in the centre regions. [59]. In contrast, the grain size and aspect ratio measurements made on the two orthogonal cross-section microstructures of the AA7003 extrusion, as part of this study, show that there is essentially no dependence of the distribution of either the size or aspect ratio of the interior non-recrystallized grains on orientation, regardless of the heat-treated condition.

The SEM/EDS examination performed on the cross-section microstructures of the AA7003 extrusion in naturally-aged T4 condition revealed the presence of larger, irregular-shaped and smaller rectangular-shaped second phase particles (Figures 5.4 & 5.5). As mentioned in the previous section, a detailed quantification of the EDS peak intensities was not attempted on the micron-sized second phase particles present in the

microstructure. However, based on the existing knowledge regarding the composition of second phase particles in AA7XXX alloys [8,13-17], it is reasonable to assume that the larger irregular-shaped phase is a $\text{Al}_{12}(\text{Fe,Mn})_3\text{Si}$ intermetallic phase, whereas the smaller rectangular-shaped phase is a Al_3Fe intermetallic phase. Note that a distinct Cu peak is not observed in the EDS analysis conducted on these second phase intermetallic particles. This observation is consistent with the microstructure characterization reported previously for AA7003 [25]. Neither of the two artificially aging heat treatments affected the shape or the major composition of these two precipitates. Again, this observation is consistent with what has been previously reported regarding the influence of heat treatment on the shape and composition of micron-sized second phase intermetallic particles present in the microstructure of AA7XXX alloys [10,16,25].

In contrast the microstructure aspects discussed thus far, the STEM/EDS analysis (Figure 5.6 & Table 5.1) of the grain boundary regions shows that significant differences exists among the three heat-treated conditions. Major differences include the density of the matrix precipitates, the density of grain boundary precipitates, the size of the SDZ and the degree of Cu enrichment (relative to the matrix) across the grain boundary region. Interestingly, these differences are found when comparing the grain boundary regions of either the coarse recrystallized surface grains or the fibrous, non-recrystallized interior grains, as a function of the heat-treated condition. Of these three, the density of matrix precipitates likely controls the resultant microhardness of the heat-treated condition. As expected, the artificially-aged T6 condition, which exhibited the highest microhardness, has the highest matrix precipitate density. Likewise, the naturally-aged T4 condition, which exhibited the lowest microhardness, had the lowest matrix precipitate density. The

microhardness of the artificially-aged paint-bake condition indicates that the time of 30 minutes is not sufficient to attain peak hardness. This observation is consistent with a reported study on the paint-bake response of Cu-lean Al-Mg-Zn alloys, in which a time of 8 hours is required at 175°C to attain peak hardness during [76].

In addition to exhibiting the highest matrix precipitate density, the artificially-aged T6 condition exhibits the highest grain boundary precipitate density. Likewise, the naturally-aged T4 condition, which exhibited the lowest matrix precipitate density, had the lowest grain boundary precipitate density. A clear positive relationship between grain boundary precipitate density and the size of the SDZ zone adjacent to the grain boundary is also evident from the STEM micrographs.

Perhaps the most surprising of all of the differences noted is the enrichment of copper observed either in the SDZ or in the grain boundary precipitate of the naturally-aged T4 condition and the artificially-aged paint-bake condition, and the lack of any copper enrichment in the artificially-aged T6 condition. This observation suggest that the relatively long soaking time associated with the artificial aging T6 heat treatment promotes the homogenization of the grain boundary region within AA7003 with respect to the Cu concentration. This hypothesis is inconsistent with the results of a relevant study, which found that, for the Cu-rich AA7150 alloy, the grain boundary precipitates in the over-aged T7 heat-treated condition had much higher Cu concentration than those in the peak-aged T6 heat-treated condition [43]. Given that the differences in the intergranular corrosion and exfoliation corrosion of AA7003 is rationalized in terms of this Cu enrichment, as discussed in more detail later, this apparent controversy needs to be resolved through further study.

6.2 EFFECT OF HEAT TREATMENT ON CORROSION BEHAVIOUR

Upon comparing the anodic polarization curves (Figure 5.7), it is clearly evident that there is a strong influence of the heat-treated condition of the corrosion potential of the extruded AA7003 microstructure. Both of the artificial aging heat treatments caused a shift in the corrosion potential in the negative (more active) direction when compared to the corrosion potential of the naturally-aged T4 condition. This shift towards a more negative corrosion potential is observed for the coarse, recrystallized surface grain structure, as well as for the fibrous, non-recrystallized interior grain structure.

This shift in corrosion potential is rationalized on the basis that both of the artificially-aged microstructures have a significantly higher density of the generic $Mg(Zn,Cu,Al)_2$ phase within the Al matrix. The electrochemical behaviour of thin films analogues of the generic $Mg(Zn,CuAl)_2$ phase has been studied in some detail in a deaerated neutral 0.5M (~3 wt.%) NaCl solution, in which the corrosion potential was measured to range from about -1420 mV_{SCE} (0 at.% Cu) to -1100 mV_{SCE} (25 at.% Cu) [13]. This range of corrosion potential, depending on the Cu content, can be significantly more negative than the corrosion potential of 978-994 mV_{SCE} exhibited by the naturally-aged (T4 condition) AA7003 extruded microstructure in the test solution utilized in this study. It follows naturally from mixed potential theory [77] that the corrosion potential should shift towards more negative values as the density (area fraction) of the more active matrix precipitate phase increases.

Unlike the influence on the corrosion potential, both artificial aging heat treatments have essentially no influence on the single breakdown potential exhibited either by the coarse recrystallized surface grain structure or the fibrous non-recrystallized

interior grain structure. Inspection of the polarized surface (Figure 5.8) reveals significant pitting corrosion, which indicates that this single breakdown potential corresponds to a pitting potential, regardless of the heat-treated condition.

Pitting is generally associated with breakdown of local passive film on the surface of the metal. In the case of aluminum alloys, pitting is influenced in large part by the presence of coarse second phase intermetallic particles. A compilation of corrosion potentials of various intermetallic phases in Al alloys shows that the intermetallics exhibit different electrochemical properties from the matrix [16]. Pits are readily found at the periphery of noble particles in Al alloys during exposure to chloride solutions [16,56,57]. The cathodic activity on the noble phases causes a local alkalinization of electrolyte resulting from the formation of hydroxyl ions as reaction product. As the protective passive film on Al is not stable in alkaline environments [78], localized breakdown would then occur adjacent to the intermetallic phase [16,54,55].

The lack of influence of the artificially-aging treatments on the pitting potential can be rationalized using this micro-galvanic cell activity theory. The SEM/EDS examination shows two major types of coarse intermetallic particles, namely, $\text{Al}_{12}(\text{Fe,Mn})_3\text{Si}$ and Al_3Fe , present in the microstructure, regardless of the heat-treated condition. The compilation of corrosion potentials for intermetallic particles in Al alloys shows that the Al_3Fe phase has a more noble corrosion potential relative to that of the AA7XXX matrix, whereas the $\text{Al}_{12}(\text{Fe,Mn})_3\text{Si}$ phase has a more active corrosion potential [16]. Since the same type of coarse intermetallic phases are present in each of the three heat-treated conditions under study, it follows that the pitting potential of each heat-treated condition of AA7003 should be similar.

The conclusion that the single breakdown potential exhibited by the AA7003 extrusion is a pitting potential is also supported by the observation that intergranular corrosion (ASTM G110) and exfoliation corrosion (ASTM G34) both initiate from corrosion pits, regardless of the heat-treated condition. Such a transition is often observed during the localized corrosion of AA7XXX alloys [52].

The heat-treated condition of the AA7003 extrusion is found to have a strong influence on the susceptibility to intergranular corrosion (Figure 5.9) and exfoliation corrosion (Figure 5.12). Of the three heat-treated conditions studied, the T6 artificially-aged condition (post weld stress relief heat treatment) exhibits the lowest susceptibility to both intergranular corrosion (ASTM G110) and exfoliation corrosion (ASTM G34). Given that both intergranular corrosion and exfoliation corrosion initiated from the base of corrosion pits, it appears as though the propagation stage in the fibrous non-recrystallized interior grain structure controls the susceptibility of the AA7003 extrusion to both of these localized corrosion forms.

From a microstructure perspective, the susceptibility of the AA7003 extrusion to intergranular corrosion and exfoliation corrosion appears to be controlled by the degree of Cu enrichment across the grain boundary region of the fibrous non-recrystallized interior grain structure. The STEM/EDS examination (Table 5.1) reveals Cu enrichment (relative to the matrix) in the SDZ in both the naturally-aged T4 condition and in the artificially-aged paint-bake cycle condition, and no Cu enrichment in the PZF in the artificially-aged T6 condition, which happens to exhibit the lowest susceptibility to these forms of corrosion. However, it is unclear at this time how the T6 heat treatment could

eliminate the Cu enrichment observed across the grain boundary region in the naturally-aged (as-extruded) condition and in the artificially-aged paint-bake cycle condition.

It is well known that the over-aged T7 condition of Cu-rich AA7XXX alloys has a lower susceptibility to intergranular corrosion and exfoliation corrosion than the peak-aged T6 condition. Although a consensus on the mechanism responsible for the lower susceptibility has yet to be attained, it is clear that over-aging tends to increase the Cu content in the generic $Mg(Zn,Cu,Al)_2$ grain boundary precipitates. These reported observations are opposite to what is reported in this study. Clearly, a more detailed examination of the grain boundary regions of the AA7003 extrusion in the various heat-treated conditions is required to help resolve this apparent discrepancy.

6.3 PROPOSED MECHANISM

The observed decreased susceptibility (extent of propagation) of the artificially-aged T6 heat-treated can again be rationalized on the micro-galvanic cell activity between the SDZ and generic $Mg(Zn,Cu,Al)_2$ grain boundary precipitates when in contact with the electrolyte within the corrosion pit. It is argued here that the transition from pitting corrosion to intergranular corrosion (including exfoliation corrosion) occurs once the coarse Al_3Fe intermetallic particle cathode has been completely undercut by the dissolving matrix at the periphery. At this point the electrical contact with the effective Al_3Fe cathode is lost and a new cathode site is required to support further anodic dissolution of the film-free pit surface. Considering the relative differences in the corrosion potentials cited for the AA7XXX matrix, SDZ and the generic $Mg(Zn,Cu,Al)_2$ grain boundary precipitates [13, 14], it is reasonable to consider a micro-galvanic cell

between the more noble SDZ (cathode) and the more active generic $Mg(Zn,Cu,Al)_2$ grain boundary precipitates (anode) is established when present at the surface of the film-free pit wall. The cell activity is expected to be mild for the artificially-aged T6 condition since there is no Cu enrichment across the grain boundaries. In contrast, the microgalvanic cell activity is expected to be significantly stronger for the naturally-aged T4 condition, since Cu is enriched in the SDZ and depleted in the generic $Mg(Zn,Cu,Al)_2$ grain boundary precipitates. In other words, a smaller potential difference (driving force) between the SDZ and the generic $Mg(Zn,Cu,Al)_2$ grain boundary precipitates is expected for the artificially-aged T6 condition because of the consistent Cu concentration across the grain boundary region. This can be represented in the Figure 6.2, explaining the transition from pitting to intergranular corrosion in terms of electrochemical cell activity between active grain boundary precipitates and noble SDZ.

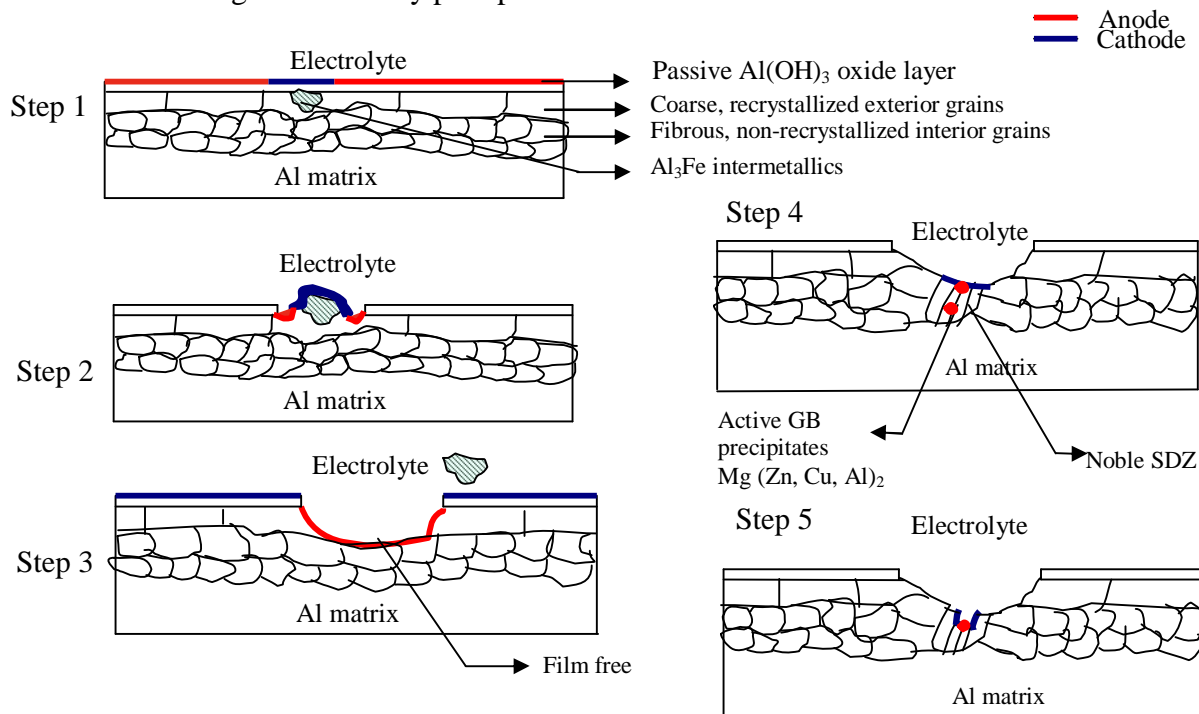


Figure 6.1 Intergranular corrosion propagation mechanism.

The intergranular propagation mechanism can be further explained by the difference in corrosion between SDZ, generic $Mg(Zn,Cu,Al)_2$ grain boundary precipitates and α matrix [13-16]. The difference in corrosion potential leads to the formation of micro-galvanic couple, which is significantly strongly active in naturally-aged T4 condition than artificially aged T6 condition. Table 2.1 [16] shows the difference in corrosion potential between α matrix, SDZ and generic $Mg(Zn,Cu,Al)_2$ grain boundary precipitates. This can be shown in Figure 6.3, representing the micro-galvanic cell formation due to difference in corrosion potentials for naturally-aged T4 and artificially aged T6 heat treated conditions.

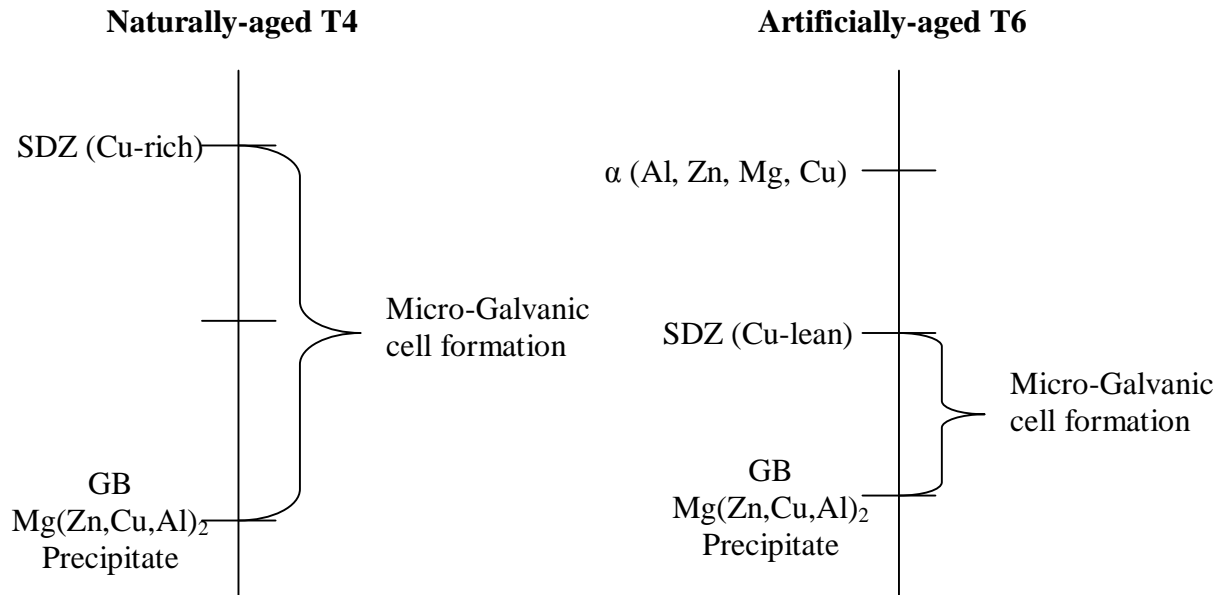


Figure 6.2 Galvanic couple formation in naturally-aged T4 and artificially-aged T6 heat treated condition.

7.0 CONCLUSIONS

The overall objective of this study is to better understand the key structure-performance relationships involved in the intergranular corrosion and exfoliation corrosion of AA7003 extrusions, as a function of the heat treatment applied. The heat treatments of interest are a naturally-aged T4 (as-extruded) condition, an artificially-aged T6 condition, and an artificially-aged automotive paint-bake condition. The adopted approach consisted of an initial detailed examination of the influence of heat treatment of the microstructure of the AA7003 extrusion, which was followed by a detailed examination of the influence of the heat-treated condition on the corrosion behaviour.

The influence of heat-treatment on the resultant microstructure was characterized using light optical microscopy, coupled with image analysis, and electron (scanning & transmission) microscopy, coupled with energy dispersive spectroscopy. Major conclusions drawn from this part of the study include the following:

- The extrusion process (naturally-aged condition) yields a dual cross-section grain structure (LT-ST & L-ST microstructures), which consist of a fibrous, non-recrystallized grain structure in the interior and a coarse recrystallized grain structure at the exterior surface. The grains, when examined in cross-section, are slightly elongated in L direction in the L-ST microstructure and along the LT direction in the LT-ST microstructure. There is no significant difference in the grain size distribution or the grain aspect ratio distribution between the two cross-section microstructures. This implies that the microstructure should be largely

isotropic. This claim is supported by the microhardness (yield strength) measurements.

- As expected, neither of the artificially aging heat treatments applied significantly modified the grain size distribution nor the grain aspect ratio distribution. Consequently, the artificially-aged condition is expected to be largely isotropic. Again, the claim is supported by the microhardness (yield strength) measurements.
- Of the two artificially-aged conditions, the T6 (representing a post weld stress relieved heat treated condition) has the higher microhardness (yield strength) than the paint-bake (PB) heat treatment cycle. This difference is consistent with the T6 condition having a higher density (volume fraction) of the strengthening η' -MgZn₂-type precipitates within the Al matrix grains.

The influence of heat treatment on the corrosion behaviour was characterized using anodic polarization measurements and ASTM standardized testing to evaluate the susceptibility resistance to intergranular corrosion (ASTM G110) and exfoliation corrosion (ASTM G34). Major conclusions drawn from this part of the study include the following:

- Both artificially aging heat treatments shift the corrosion potential of the AA7003 extrusion in the negative direction, regardless of the grain structure (surface verse interior). The shift can be rationalized on the micro-galvanic cell activity established between the noble Al matrix grains and the more active strengthening

η' -MgZn₂-type precipitates within the Al matrix grain. The negative shift in the corrosion potential results from the increased density (surface area fraction) of the more active strengthening η' -MgZn₂-type precipitates within the Al matrix grain observed in the artificially-aged heat treated conditions relative to the naturally-aged condition.

- Unlike the influence on the corrosion potential, both artificially aging heat treatments have essentially no influence on the single breakdown potential, regardless of the grain structure (surface verse interior). This single breakdown potential corresponds to a pitting potential, regardless of the heat-treated condition. The lack of influence can be rationalized on the micro-galvanic cell activity established between the more noble second phase intermetallic particles and the more active Al matrix grains, which leads to a localized breakdown of the protective passive film on the Al matrix grains. The similar breakdown potential results from the similar composition of the intermetallic particles, namely Al₃Fe, present in the microstructure, regardless of the heat-treated condition.
- The T6 artificially-aged condition (post-weld stress-relief heat treatment) of the AA7003 extrusion exhibits the lowest susceptibility to both intergranular corrosion (ASTM G110) and exfoliation corrosion (ASTM G34). The observed decreased susceptibility (extent of propagation) can again be rationalized on the micro-galvanic cell activity between the PZF and generic Mg(Zn,Cu,Al)₂ grain boundary precipitates when in contact with the electrolyte within the corrosion pit. The transition from pitting corrosion to intergranular corrosion (including exfoliation corrosion) occurs once the coarse Al₃Fe intermetallic particle cathode

has been completely undercut by the dissolving matrix at the periphery. At this point the electrical contact with the effective Al_3Fe cathode is lost and a new cathode site is required to support further anodic dissolution of the film-free pit surface. The new site is created by the micro-galvanic cell established between the more noble PZF (cathode) and the more active generic $\text{Mg}(\text{Zn},\text{Cu},\text{Al})_2$ grain boundary precipitates (anode) is established when present at the surface of the film-free pit wall. The cell activity is mild for the artificially-aged T6 condition since there is no Cu enrichment across the grain boundaries. In contrast, the micro-galvanic cell activity is significantly stronger for the naturally-aged T4 condition, since Cu is enriched in the PZF and depleted in the generic $\text{Mg}(\text{Zn},\text{Cu},\text{Al})_2$ grain boundary precipitates.

These conclusions have several major implications with respect to the performance of automotive bumper assemblies fabricated using AA7003 extrusions. First, either of the artificially aging heat treatments that could be applied post-assembly, namely a post-weld stress relief heat treatment (T6) and a paint-bake cycle heat treatment (PB), increase the hardness (strength) relative to the naturally-aged (as-extruded) condition (T4). The increased strength can permit the utilization of thinner wall extrusions while maintaining a similar level of energy absorption (crashworthiness), which results in a weight savings. Second, the combined effect of a similar breakdown potential and a more negative corrosion potential, decreases the susceptibility to pitting corrosion, since a larger extent of anodic polarization is required for pits to initiate, and thus for intergranular corrosion and exfoliation corrosion to initiate. Third, of the two

alternative assembly routes, the one in which AA7003 bumper beam assembly is supplied with the crush cans welded in position, complete with a post-weld, stress-relief heat treatment (T6), is expected to have the lower susceptibility to intergranular corrosion and exfoliation corrosion.

8.0 REFERENCES

1. J.T. Staley and D.J. Lege, Journal de Physique IV, Vol. 3, No. C7, pp. 179-190 (1993).
2. H.A. Clausen, O.S. Hopperstad and M. Langseth, Journal of Materials Processing Technology, Vol. 102, Issues 1-3, pp. 241-248 (2000).
3. S. Kokkula, M. Langseth, O.S. Hopperstad, and O-G Lademo, International Journal of Crashworthiness, Vol. 11, Issue 4, pp. 299-316 (2006).
4. K.O. Pedersen, O.G. Lademoa, T. Berstad, T. Furu, O.S. Hopperstad, Journal of Materials Processing Technology, Vol. 200, pp. 77-93 (2008).
5. Y. Chen, K.O. Pedersen, A.H. Clausen, and O.S. Hopperstad, Materials Science and Engineering: A, Vol. 523, Issues 1-2, pp. 253-262 (2009),
6. W. S. Miller, L. Zhuang, J. Bottema, A. J. Wittebrood, P. De Smet, A. Haszler and A. Vieregg, Materials Science and Engineering A, Vol. 280, Issue 1, pp. 37-49 (2000).
7. M. Bertram, K. Buxmann and P. Furrer, The International Journal of Life Cycle Assessment, Vol. 14, Issue 1, pp. 62-69 (2009).
8. M.O. Speidel, Metallurgical Transactions, Vol. 6A, pp. 631 (1975).
9. D.G. Evans, P.W. Jeffrey, and U.R. Evans Conference on Localized Corrosion, R.W. Staehle, B.F. Brown, J. Kruger, A. Agarwal (Editors), NACE-3, Houston, TX (1974).
10. N.J.H. Holroyd, Environment-Induced Cracking of Metals, R.P. Gangloff, M.B. Ives (Editors), pp. 311, NACE, Houston, TX (1990).
11. S. Maitra and G.C. English, Materials Transactions A, Vol. 12, pp. 535 (1981).
12. J.K. Park, A.J. Ardell, Acta Metallurgia, Vol. 39, pp. 591 (1991).

13. T. Ramgopal, P. Schmutz and G.S. Frankel, Journal of the Electrochemical Society, Vol. 148, pp. B348 (2001).
14. T. Ramgopal, P.I. Gouma and G.S. Frankel, Corrosion, Vol. 58, pp. 687 (2002).
15. Q. Meng and G.S. Frankel, Journal of the Electrochemical Society, Vol. 151, pp. B271 (2004).
16. N. Birbilis, R.G. Buchheit, Journal of the Electrochemical Society, 152 (4), pp. B140-B151 (2005).
17. I.J. Polmear, Light Alloys, 3rd Edition, Arnold, London (1995).
18. N.A. Belov, A.A. Aksenov, D.G. Eskin, In: J.N. Fridlyander, D.G. Eskin, Editors: Taylor and Francis, London, pp. 15 (2002).
19. A.K. Mukhopadhyay, V.V. Rama Rao, C.R. Chakravorty, Mater. Sci. Forum, Vol. 217-222, pp. 1617 (1996).
20. X.M. Li, M.J. Starink, Materials Science Technology, 17, pp. 1324 (2001).
21. Ji-Gang Yang, Bin-Lung Ou, Scandinavian Journal of Metallurgy, Vol. 30, pp. 158-167 (2001).
22. M. Gao, C.R. Feng, R.P. Wei, Metall. Mater. Trans. A 29A, pp. 1145 (1998).
23. F. Andreatta, H. Terryn, J.H.W de Wit, Corrosion Science, Vol. 45, pp. 1733-1746 (2003).
24. P.S. Pao, C.R. Feng, S.J. Gill, Corrosion, 56, pp. 1022 (2000).
25. Hoon Chaol, Hyung-Ho Jo, Kyung-Whoan Lee, Young-Jig Kim, Journal of Materials Processing Technology, Vol. 130–131, pp. 407–410 (2002).
26. M. Puiggali, A. Zielinski, J.M. Olive, E. Renauld, D. Desjardins, M. Cid, Corros. Sci. Vol. 40, pp. 805 (1998).

27. R.G. Hamerton, H. Cama, M.W. Meredith, Materials Science Forum, 331-337, pp. 143, (2000).
28. E.A. Starke, J.T. Staley, Prog. Aerosp. Sci. 32, pp. 131 (1996).
29. J.D. Robson, P.B. Prangnell, Acta Mater. Vol. 49, pp. 599 (2001).
30. T.S. Srinivasan, S. Sriram, D. Veeraraghavan, V.K. Vaudevan, J. Mater. Sci., 32, pp. 2883 (1997).
31. R. Ayer, J.Y. Koo, J.W. Steeds, B.K. Park, Metall. Trans. Vol. A 16A, pp. 1925 (1985).
32. M. Kanno, I. Araki, Q. Cui, Materials Science and Technology, Vol. 10, No. 7, pp. 599-603 (1994).
33. H. Yoshida, Y. Baba, Trans. Jpn. Ins. Met. 23, pp. 620 (1982)
34. Dong Seok Park, Soo Woo Nam, Journal of Materials Science, Vol. 30, pp. 1313-1320 (1995).
35. Lendvai, Materials Science Forum, Vols. 217-222 (1996), pp. 43-56.
36. S.K. Maloney, K. Kono, I.J. Polmear, S.P. Ringer, Scr. Mater. 41, pp. 1031 (1999).
37. K. Stiller, P.J. Warren, V. Hansen, Mater. Sci. Eng. A A270, pp. 55 (1999)
38. T. Engdahl, K. Stiller, P.J. Warren, V. Hansen, Mater. Sci. Eng. A A327, pp. 59 (2002)
39. D.A. Porter, K.E. Easterling, 'Phase Transformtions in Metals and Alloys', Van Nostrand Reinhold (International) Co. Ltd., pp. 291, 1981.
40. Elwin L. Rooy, ASTM Handbook, Vol. 2 (Formerly 10th Edition Metals Handbook), 'Properties & Selection: Non-Ferrous and Special-Purpose Materials', pp. 3-122.
41. Richard H. Stevens, ASTM Handbook, Vol. 9, (Formerly 9th Edition Metals Handbook), 'Metallography & Microstructure', pp. 351-388.
42. J.K Park, A.J. Ardell, Acta Metall., 34, pp. 2399 (1986).

43. J.K Park, A.J. Ardell, Metall. Trans., A 15A, pp. 1531 (1984).
44. L.F. Mondolfo, Metall. Rev., 16, pp. 95 (1971).
45. A. Joshi, C.R. Shastry, M. levy, Metall. Trans., A 12A, pp. 1081 (1981).
46. A. Bigot, F. Danoix, P. Auger, D. Blavette, A. reeves, Mater. Sci. Forum, 217-222, pp. 695 (1996).
47. M. Tanaka, R. Dif, T. Warner, Mater. Sci. Forum, 396-402, pp. 1449 (2002).
48. A. Barbucci, G. Cerisola, G. Bruzzone, A. Szccone, Electrochimica Acta, Vol. 42, No. 15, pp. 2369-2380 (1997).
49. T.G. Dunford, B.E. Wilde, In: M.E. Blum, P.M. French, R.M. Middleton, G.F. Vander Voort Editors, Microstructural Science, Vol. 15, ASM International, Metals Park, p. 263 (1987).
50. V. Hansen, K. Stiller, G. Waterloo, J. Gjonnes, X.Z. Li, Mater. Sci. Forum, Vol. 396-402, pp. 815 (2002).
51. Denny A Jones, Principles and Prevention of Corrosion, 2nd edition, Prentice Hall, INC., pp. 9-21 (1996).
52. J.K Park, A.J. Ardell, Scr. Metall., 22, pp. 1115 (1988).
53. E.H.Hollingsworth, H.Y.Hunsicker, ASM handbook (Formerly 9th Edition Metals Handbook), Vol. 13, ‘Corrosion of Aluminum and Aluminum Alloys’, pp. 583-609.
54. C.W. Bartges, J. Mater. Sci. Lett. 13, pp. 776 (1994).
55. P. Guyot, L. Cottignies, Acta Mater. 44, pp. 4161 (1996).
56. Iduvirges L. Muller, Jose R. Galvele, Corrosion Science, Vol. 17, pp. 995 (1977)
57. N. Birbilis, M.K. Cavanaugh, R.G. Buchheit, Corrosion Science, Vol. 48, pp. 4202-4215 (2006).
58. B.W. Lifka and D.O. Sprowls, ASTM STP 516, pp. 120 (1972).

59. E.H. Dix Jr., American Institute of Mining and Metallurgical Engineers Transactions, 137, pp. 11-40 (1940).
60. J.R. Galvele and S.M. De De Micheli, Corrosion Science, Vol. 10, pp. 795-807 (1970).
61. R.G. Buchheit, J.P. Moran, and G.E. Stoner, Corrosion Science, Vol. 50(2), pp. 120-130 (1994).
62. T.S. Huang, G.S. Frankel, Corrosion Science Section, NACE International, Vol. 63, No. 8, pp. 731-743 (2007).
63. S. Maitra and G.C. English, Metallurgical Transactions A, 13A, 161-166 (1982).
64. M.J. Robinson, N.C. Jackson, Corrosion Science, 41, pp. 1013-1028 (1999).
65. E. Ghali, 'Aluminum and Aluminum Alloys' in Uhlig's Corrosion Handbook, Editors R.W.Revie, New York, NY: John Wiley & Sons, INC., pp. 677-716 (2000).
66. L.L. Shreir, F.R.I.C and F.I.M, 'Corrosion' 2nd Edition, Editors L.G Shreir, Newnes-Butterworth (1976).
67. E. Mattsson, L.O. Gullman, L. Knutsson, R. Sundberg, B. Thundal, British Corrosion Journal, 7, pp. 73-83 (1971).
68. D. Adenis, A. Guilhaudis, Memoires Scientifiques de la Revue de Metallurgie, 64(10), pp. 877-888 (1967).
69. G. Bassi, J.J. Theler, Zeitschrift fur Metalkunde, 58(3), pp. 178-184 (1969).
70. H.A. Holl, Journal of the Institute of Metals, Vol. 97(200), pp. 200-205 (1969).
71. D. McNaughtan, M. Worsfold, M.J. Robinson, Corrosion Science, 45, pp. 2377-2389 (2003).
72. M. J. Robinson, Corrosion Science, Vol. 22(8), pp. 775-790 (1982).

73. Xinyan Zhao and G. S. Frankel, Corrosion Science Section, NACE International, Vol. 62, pp. 256-266 (2006).
74. Anonymous, "International Alloy Designation and Chemical Corporation Limits for Wrought Aluminum and Wrought Aluminum Alloys", The Aluminum Association, Inc., Arlington, VA (February 2009).
75. O.G. Lademo, K.O. Pedersen, T. Berstad, T. Furu, O.S. Hopperstad, European Journal of Mechanics A/Solids, Vol. 27, pp. 116 (2008).
76. D.C. Balderach, J.A. Hamilton, E. Leung, M.C. Tejeda, J. Qiao, E.M. Taleff, Materials Science and Engineering A, Vol. A399, pp. 194 (2003).
77. M. Stern & A.L. Geary, J. of the Electrochemical Society, Vol. 104, No. 1, 56-63 (1957).
78. M. Pourbaix, Atlas of electrochemical equilibria in aqueous solutions, Houston, TX, NACE (1974).
79. "Standard Test Methods for Determining Average Grain Size", in Annual Book of ASTM Standards, Philadelphia, PA: The American Society for Testing and Materials, E 112-96 (Reapproved 2004).
80. "Standard Practice for Evaluating Intergranular Corrosion Resistance of Heat Treatable Aluminum Alloys by Immersion in Sodium Chloride + Hydrogen Peroxide Solution", in Annual Book of ASTM Standards, Philadelphia, PA: The American Society for Testing and Materials, G 110-92 (Reapproved 2003).
81. "Standard Practice for Exfoliation Corrosion Susceptibility in 2XXX and 7XXX Series Aluminum Alloys (EXCO Test)", in Annual Book of ASTM Standards,

Master's Thesis – C. Krishnan McMaster – Materials Science and Engineering 2011

Philadelphia, PA: The American Society for Testing and Materials, G 34-01
(Reapproved 2007).

APPENDIX 1

STEM/EDS MICROGRAPHS AND LINE SCANS SHOWING EFFECT OF HEAT TREATMENT CONDITIONS & MICROSTRUCTURE

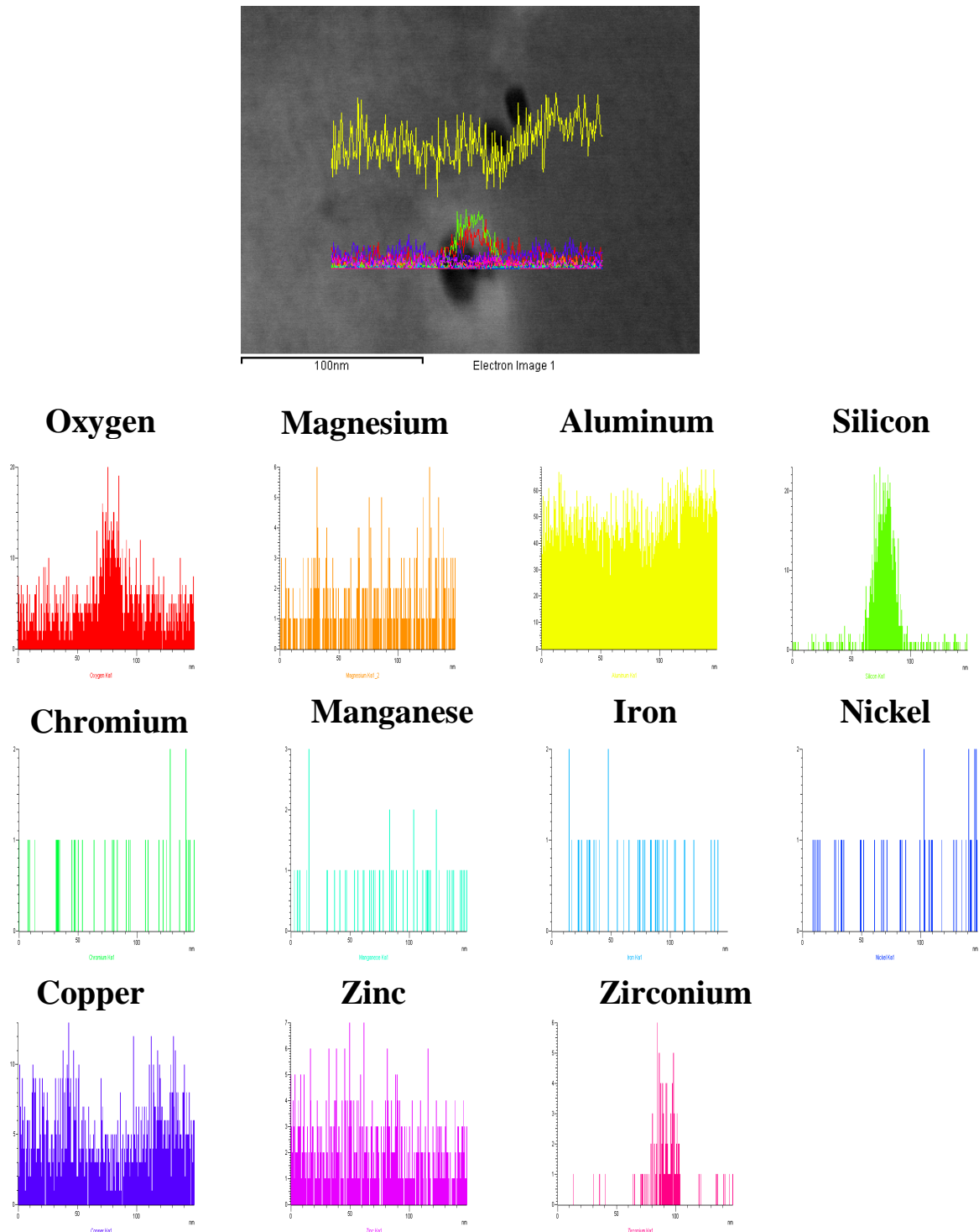


Figure 1 STEM/EDS scans for naturally aged as-received T4 coarser grain microstructure

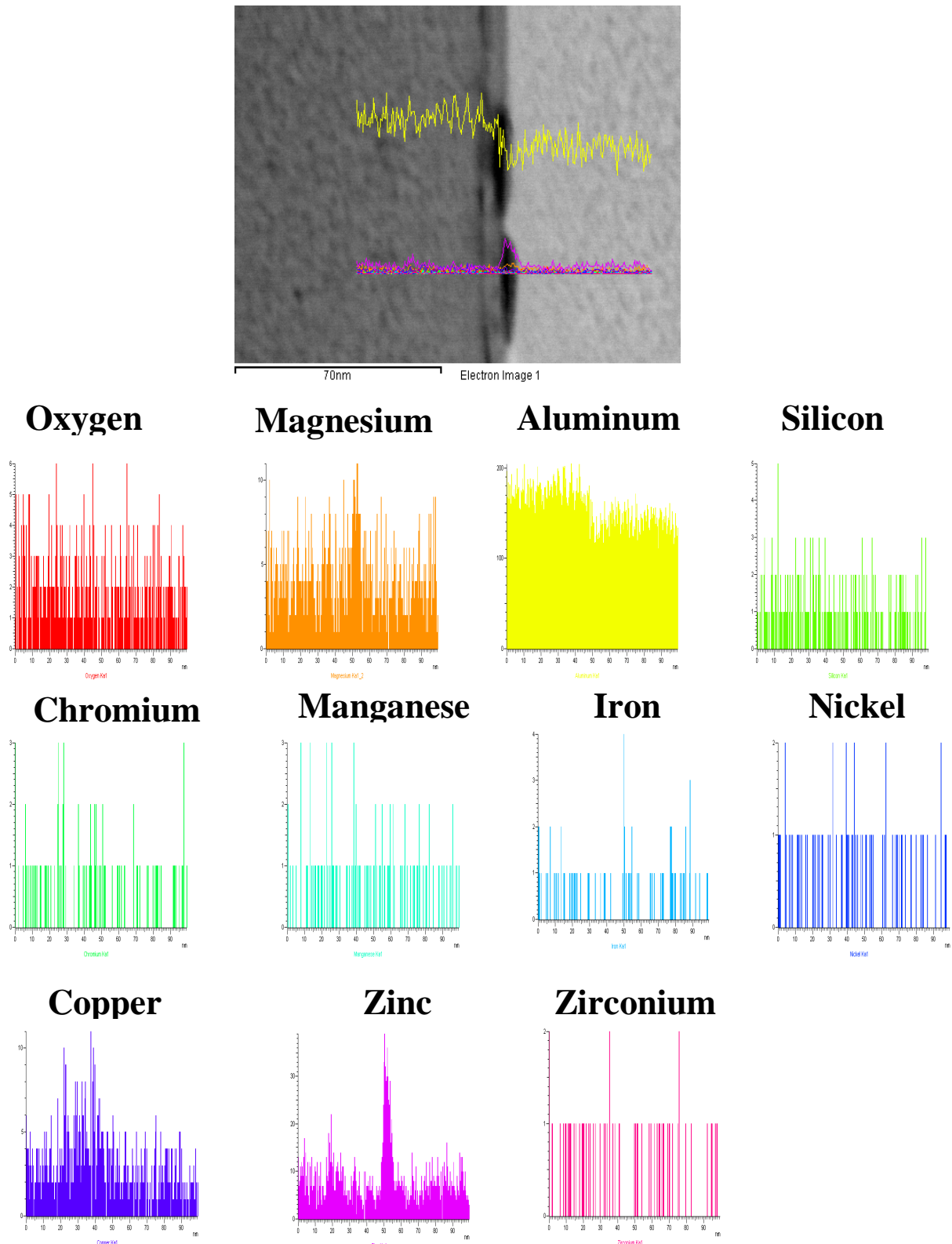


Figure 2 STEM/EDS scans for naturally aged as-received T4 finer grain microstructure

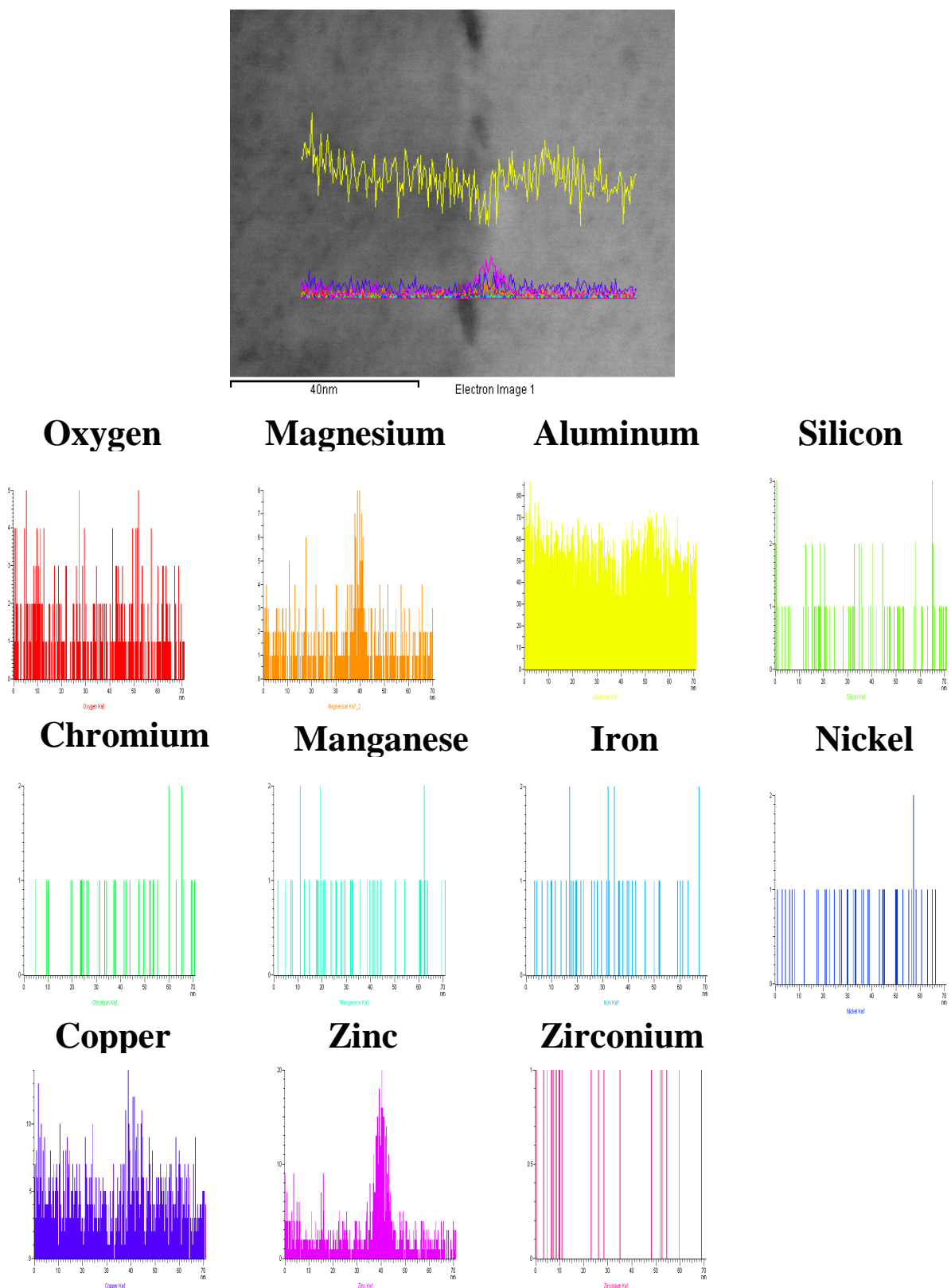


Figure 3 STEM/EDS scans for simulated paint bake PB coarser grain microstructure

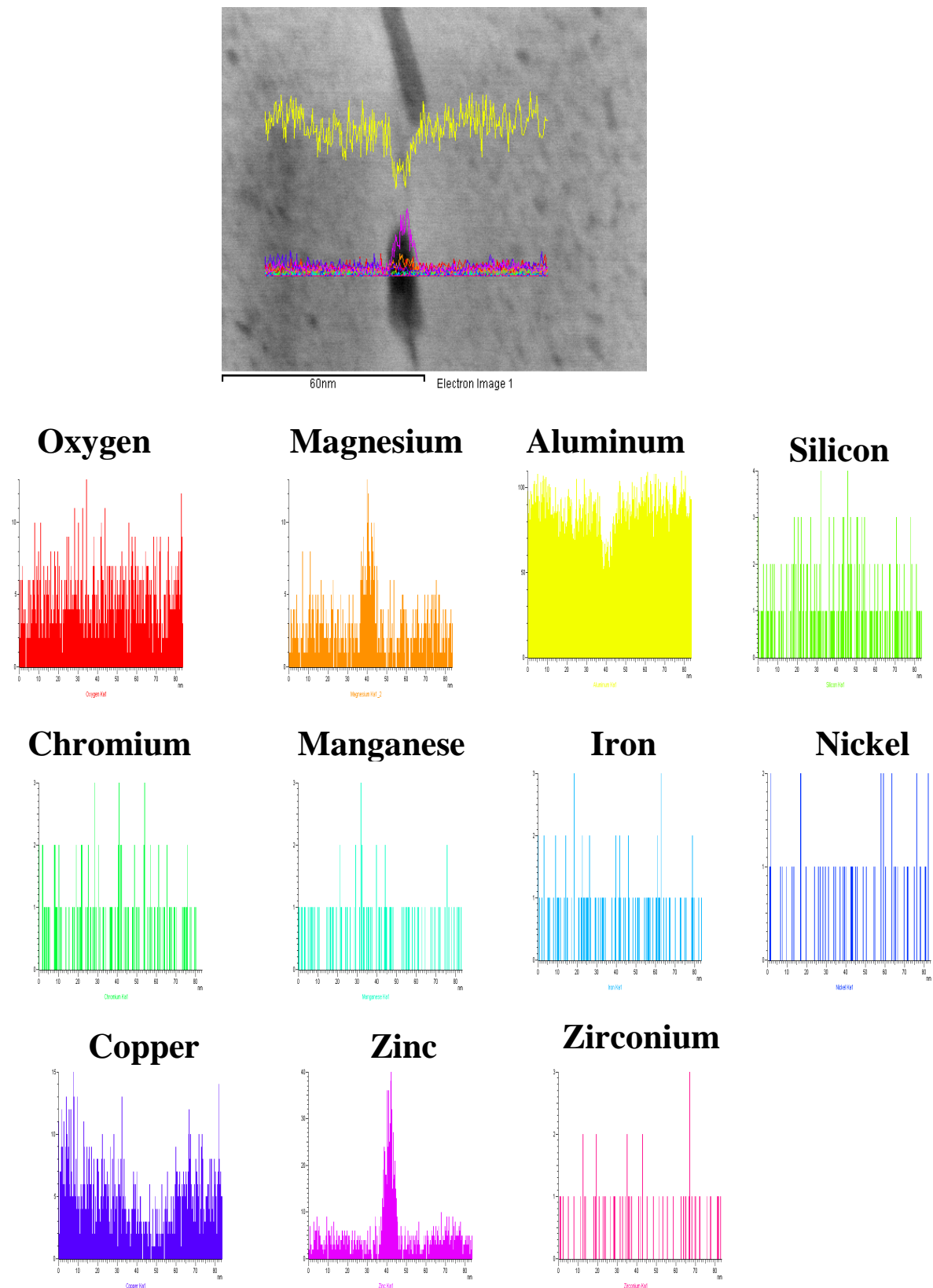
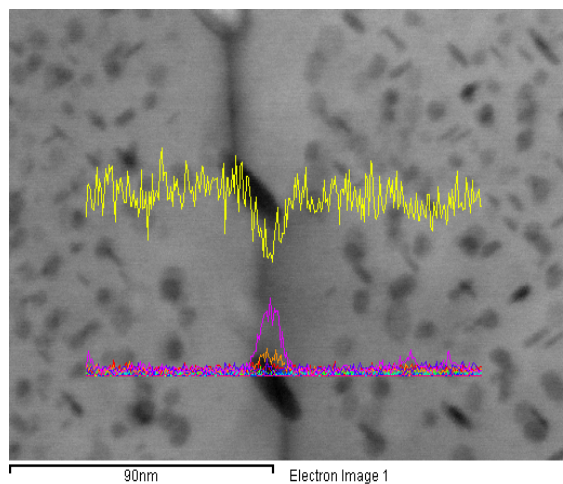
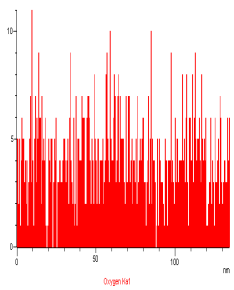


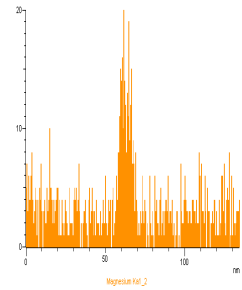
Figure 4 STEM/EDS scans for simulated paint bake PB finer grain microstructure



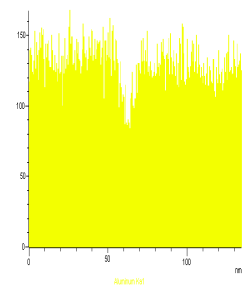
Oxygen



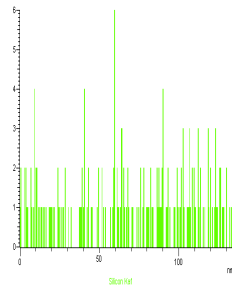
Magnesium



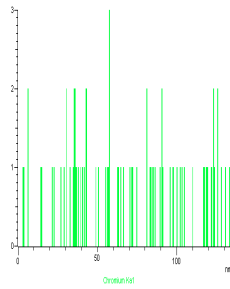
Aluminum



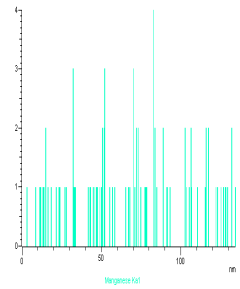
Silicon



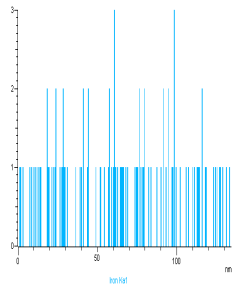
Chromium



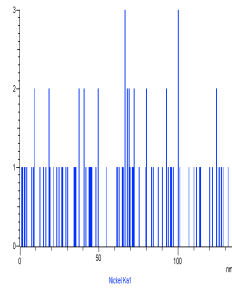
Manganese



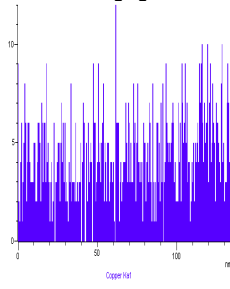
Iron



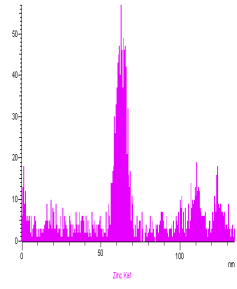
Nickel



Copper



Zinc



Zirconium

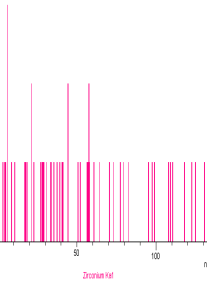


Figure 5 STEM/EDS scans for artificially aged T6 coarser grain microstructure

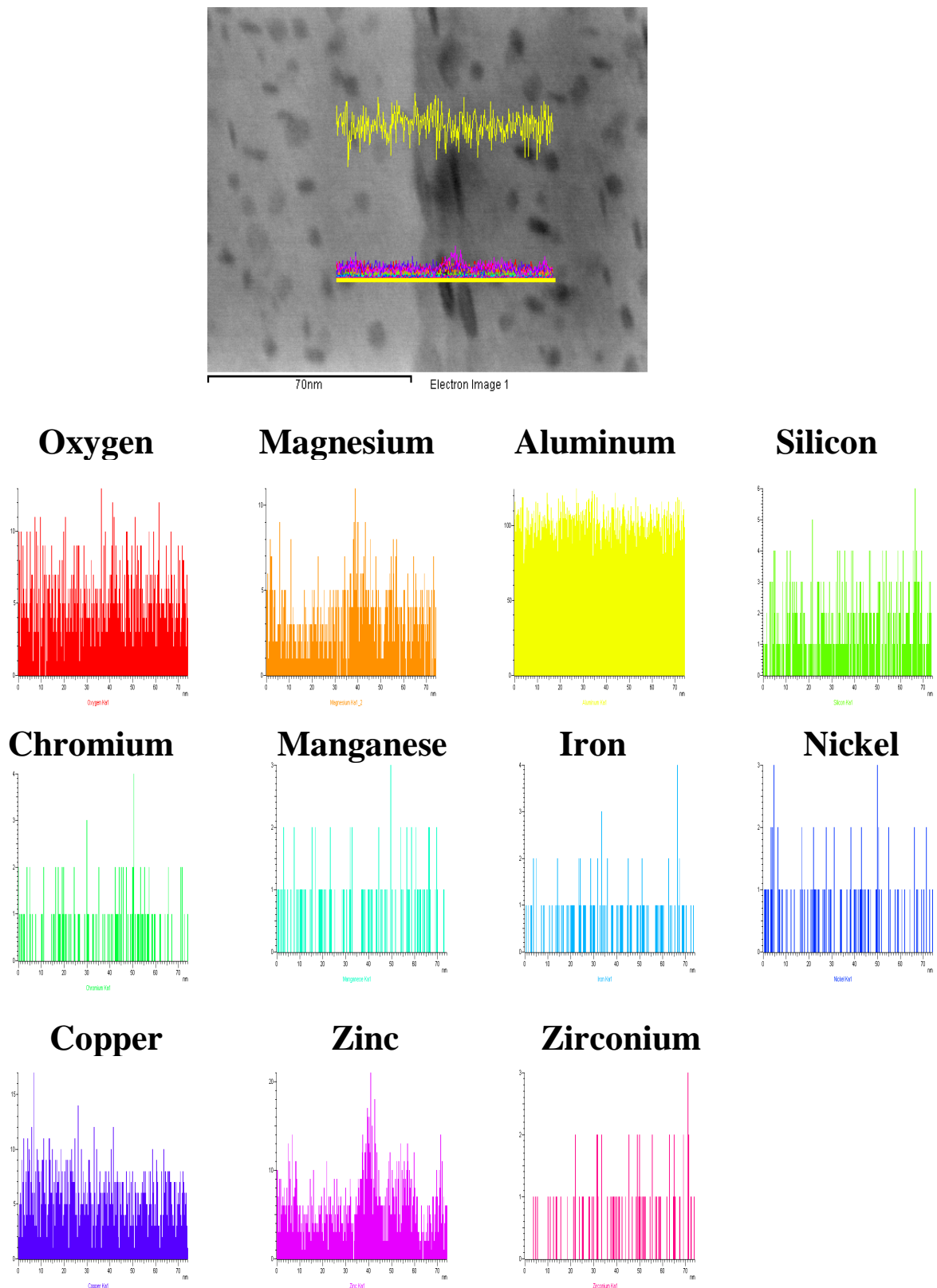


Figure 6 STEM/EDS scans for artificially aged T6 coarser grain microstructure